Thin–Walled Structures 224 (2026) 114673

Contents lists available at ScienceDirect

Thin-Walled Structures

journal homepage: www.elsevier.com/locate/tws

Full length article

Theoretical-experimental investigation on mechanical response of Al honeycomb sandwich under static compression and high-velocity impact

Raffaele Barbagallo [a], Giuseppe Bua [a], Girolamo Costanza [b], Fabio Giudice [a,*], Giuseppe Mirone [a], Andrea Sili [c], Maria Elisa Tata [b]

[a] Department of Civil Engineering and Architecture, University of Catania, Via Santa Sofia 64, 95123 Catania, Italy
[b] Department of Industrial Engineering, University of Roma Tor Vergata, Via del Politecnico 1, 00133 Roma, Italy
[c] Department of Engineering, University of Messina, Contrada di Dio, 98166 Sant'Agata, Messina, Italy

ARTICLE INFO

Keywords:
Al honeycomb sandwich panel
Quasi-static compression
High-velocity impact behavior
Perforation modelling
Ballistic limit
Energy absorption
Impact force

ABSTRACT

This paper reports a theoretical-experimental investigation aimed at characterizing the penetration behavior and ballistic limit, the energy absorption capabilities, and the impact force attenuation effect of an Al alloy sandwich panel with honeycomb core 50 mm thick, under normal impact by spherical projectiles. The analytical model used to estimate the ballistic limit has been developed according to the energy conservation-based approach, which allows to evaluate the effect of dissipation mechanisms through the elements constituting the sandwich panel. The experimental investigation has been conducted under quasi-static and high-velocity impact conditions (150–250 m/s), characterizing the out-of-plane compressive behavior and the dynamic response (ballistic limit, absorbed energy, impact force). The theoretical and experimental investigations as a whole outline an integrated approach where analytical modeling, calibrated and validated by experimental results, can be adapted to each specific application, and allows to characterize and predict the potential of the honeycomb core as an effective element for energy dissipation, and impact force attenuation, so to define the actual role for the overall penetration behavior. As main results of the investigation, for the starting configuration of the sandwich a ballistic limit of 195 m/s, an average value of energy absorption of 40.37 J, with about only 15% due to the honeycomb, and an average value of maximum impact load of 0.776 kN has been found, with substantial consistency between experimental and theoretical results. Projections by varying the main geometric parameters of the honeycomb allow to define high-potential conditions for energy absorption increase and further impact force attenuation.

1. Introduction

In recent years, due to properties such as thermal and acoustic insulation, good bending stiffness and resistance to crash and impact, Al-based composite sandwich structures have found widespread adoption as structural elements in the aeronautical [1], shipbuilding [2], railroad cars [3] and high-performance vehicle industry [4]. The aim is to use structural elements with high bending stiffness and at the same time a reduced weight compared to traditional materials. A sandwich structure consists of a central core and two facesheets, also called skins, made of metals or fiber-reinforced laminates and responsible for the mechanical properties [5]. The core is made of a low-density material to ensure lightness, and hold the facesheets together transferring loads to them. It allows to obtain greater thicknesses between the facesheets, increasing the section's moment of inertia, as well as absorbing energy in static condition, through densification due to the cell collapse in the case of foam core [6], or by progressive crumpling of the cell walls in honeycomb panels at low velocity impact [7].

The variety of constructive solutions adopted for sandwich structures is ever-increasing [3]. Investigations into the potential of multilayered solutions with widely diversified properties, obtained through the combination of composite materials of various nature [8] and the use of new advanced manufacturing processes [9], are promoted. However, honeycomb remains one of the most common types of structure studied and used as a “core”, with hexagonal or more complex cell geometry [10]. With density between 20–200 kg/m^3, these structures are today produced using different materials: reinforced and non-reinforced polymers, metals. The use of metallic materials has proven particularly fruitful in the development of innovative honeycomb-based

* Corresponding author.
E-mail addresses: raffaele.barbagallo@unict.it (R. Barbagallo), giuseppe.bua@phd.unict.it (G. Bua), costanza@ing.uniroma2.it (G. Costanza), fabio.giudice@unict.it (F. Giudice), giuseppe.mirone@unict.it (G. Mirone), andreamariano.sili@unime.it (A. Sili), elisa.tata@uniroma2.it (M.E. Tata).

https://doi.org/10.1016/j.tws.2026.114673
Received 4 November 2025; Received in revised form 20 January 2026; Accepted 13 February 2026
Available online 13 February 2026
0263-8231/© 2026 The Author(s). Published by Elsevier Ltd. This is an open access article under the CC BY-NC-ND license (http://creativecommons.org/licenses/by-nc-nd/4.0/).

Nomenclature

a, p	Parameters of Recht-Ipson model
AE	Absorbed kinetic energy
A_{ng}	Negative acceleration of the projectile through the panel
A_s	Effective sliding surface between honeycomb and second facesheet
C	Shape factor for Taylor's formula
D	Minor size of honeycomb cell
D_{av}	Average diameter of honeycomb cell
E_{s_hc}	Fracture energy per unit area of honeycomb material
F_{imp}	Impact force
F_{imp_max}	Maximum impact force
h	Facesheet thickness
H	Honeycomb core thickness
h_1	Honeycomb wall thickness
m_p	Projectile mass
m_{pl}	Plug mass (generalized)
q_{cr}	Static crushing strength of the honeycomb
q_{cr_d}	Dynamic crushing strength of the honeycomb
q_{sh}	Static shear strength of the honeycomb
q_{sh_d}	Dynamic shear strength of the honeycomb
r_p	Projectile radius
t_{in}	Time required to the projectile for traveling from the rear end of the divertor to the front face of the first facesheet
t_{out}	Time required to the projectile for traveling from the rear side of the perforated second facesheet to the fixed endplate of containment chamber
T_{cr}	Crossing time of the projectile through the panel
U*	Specific absorbed energy
v	Specific volume of sandwich panel
V_o	Projectile velocity at impact with first facesheet
V'_{bl_hc}	Corrected ballistic limit of the bare honeycomb
V_{bl}	Ballistic limit
V_{bl_hc}	Ballistic limit of the bare honeycomb
V_{bl_max}	Maximum value of the ballistic limit
V_{bl_min}	Minimum value of the ballistic limit
V_{imp}	Impact velocity (generalized)
V_{r1}	Projectile residual velocity after perforation of first facesheet
V_{r2}	Projectile residual velocity after perforation of honeycomb core
V_{r3}	Projectile residual velocity after perforation of second facesheet
V_{res}	Residual velocity (generalized)
w_1	Transverse deflection of first facesheet after perforation
W_f	Fracture work dissipation (generalized)
W_{f1}	Fracture work dissipation due to first facesheet perforation
W_{f3}	Fracture work dissipation due to second facesheet perforation
W_i	Work dissipated due to the interaction between the facesheet and the core (generalized)
W_{i12}	Work dissipated due to the interaction between the first facesheet and the core
W_{i23}	Work dissipated due to the interaction between the core and the second facesheet
W_p	Plastic work dissipation (generalized)
$W_{p1.1}$	Plastic work dissipation due to first facesheet deformation (bending neglected)
$W_{p1.2}$	Plastic work dissipation due to first facesheet bending
W_{p2}	Plastic work dissipation due to honeycomb perforation
W_{p3}	Plastic work dissipation due to second facesheet deformation
W_{Si}	Overall energy dissipation for i-th perforation stage (i = 1,2,3)
W_{SP}	Total energy dissipation due to the complete perforation of sandwich panel
ε^*_d	Strain corresponding to maximum energy absorption efficiency
ε_{cr}	Necking strain of the facesheet material
ε_u	Ultimate strain
η^*_{max}	Maximum energy absorption efficiency
η	Reduction factor for projectile radius
ρ_1	Radial extent of first facesheet deformation after perforation
ρ_2	Radial extent of second facesheet deformation after perforation
σ^*_m	Plateau stress
σ^*_{pk}	Peak stress
σ_{o_i}	Assumptions for average flow stress calculation (i = 1,2,3,4)
σ_{o_fs}	Flow stress of the facesheet material
$\sigma_{o\_fs\ max}$	Flow stress of the facesheet material (maximum value)
$\sigma_{o\_fs\ min}$	Flow stress of the facesheet material (minimum value)
σ_{o_hc}	Flow stress of the honeycomb material
σ_u	Ultimate strength
σ_y	Yield strength
τ_{s_b}	Shear strength of the bonding between honeycomb and second facesheet
τ_{s_hc}	Shear strength of honeycomb material
ξ_s	Average sliding distance between honeycomb and second facesheet
ψ	Reduction factor for ultimate strength (flow stress calculation)

structures [11], maintaining an important role even in the most advanced applications [12]. Aluminum, on the other hand, is the most widespread material in metal honeycomb.

Honeycomb panels have been the subject of numerous research studies, mostly for their mechanical properties. The compressive behavior of metallic honeycombs is strongly influenced by the geometry of the cell, by the properties of the material constituting the cell wall and, in particular, by the relative density (for a comprehensive review on this topic see [13]). In more general terms, to obtain maximum rigidity and resistance to bending, the weight of the honeycomb must be 50–66.7% of the weight of the whole sandwich panels [14].

In addition to their wide use as structural elements, which combine effectively high strength, stiffness, and lightweight, sandwich honeycomb panels have also gained a significant role in civil applications requiring high energy absorption under impact and perforation conditions. In this field they have shown their potential as protective components for aircrafts and aerospace vehicles, high-speed trains, and generally all structures that can be subject to bird strike, or the impact from runaway debris and hailstones, which can result in a variety of damage forms, from facesheet indentation to full panel perforation, strictly influenced by the interaction modes between penetrating bodies and the internal structure of the honeycomb core [15–19].

The perforation and ballistic impact behaviors of sandwich panels with metallic honeycomb cores have been studied extensively for several decades. The ballistic limit and the energy dissipation mechanisms in the case of auxetic honeycomb have also been investigated [20, 21].

This field of research was based on theoretical studies and ballistic tests conducted with different projectile shapes, obtaining the ballistic limits and the characterization of perforation behavior. It has its roots in the research on quasi-static behavior of the metallic honeycomb, based on the seminal works by McFarland [22] and Wierzbicki [23], and their further development [24–27], which were accompanied by investigations specifically oriented to the ballistic response [28–31].

In some cases, particular attention has been given to the role of analytical modelling in supporting experimental investigation [32,33]. These approaches are based on energy conservation principle, assuming that the kinetic energy of the projectile is dissipated in the various mechanisms of plastic deformation that arise when crossing the honeycomb (folding and crushing of the structure, tearing and delamination of cell walls, shearing of the plug).

A comprehensive overview of the extensive investigation conducted on the main aspects of the crushing behavior of honeycomb structures (quasi-static and dynamic studies on out-of-plane and in-plane loading, bending and fracture analysis, low, medium and high-velocity impacts, blast loading), can be found in [34]. Including approaches to mathematical modeling and experimental investigations, this overview also highlights the contribution to the development of this field of research given by the use of numerical analysis of honeycomb behavior.

While the behavior under impact and penetration of bare honeycomb structures has been extensively studied also from an analytical point of view, the same cannot be said for the sandwich panel as a whole, consisting of honeycomb core sandwiched between facesheets.

Impact response phenomena in the ballistic field on solid plates, studied for a long time and widely developed [35,36], has provided important support in this regard. Some models conceived for plates perforation are still commonly used to extrapolate information on the behavior of the entire sandwich panel. This is the case of the Recht–Ipson model [37], conceived to estimate the residual velocity of projectiles with high length/diameter ratio impacting thin plates by using energy consideration, which in a generalized form is commonly used for the calculation of the ballistic limit by interpolation of experimental data also in the case of cellular structures such as honeycombs [32].

Since the main difficulty in extending the findings on the ballistic behavior of the two separate elements (plates and core) concerns the complexity of the interactions between these elements of the panel, an analytical model for the analysis of perforation process and the calculation of the ballistic limit for aluminum sandwich structures, which takes into account these interactions, has been proposed [38]. Also this type of modelling is based on energy conservation principles, an approach that allows also to analyze the partition of absorbed energy during the phases of penetration process. As similar proposals, mathematical models for high-velocity impact in foam cored sandwich and honeycomb cored panels with composite facesheets have also been developed [39,40].

Between the metallic solutions, the case of impact effects and ballistic behavior of aluminum alloys sandwich panels with hexagonal cell core has received specific attention and has been studied in recent years mainly by experimental and numerical approaches.

A numerical model, calibrated on experimental data, has been developed by Kolopp et al. [41] to study the ballistic response of sandwich structures subject to medium-velocity impacts (120 m/s) of spherical projectile, implementing elasto-plastic and strain-rate dependent behavior, and considering several combinations of aluminum alloys for facesheets and honeycomb, to establish correlations between materials, geometrical parameters, and the sandwich performances. Sun et al. [42] investigated the effects of facesheet thickness, core height, cell wall thickness and cell size of honeycomb on the impact behavior of the whole panel. Deformation and failure mechanisms were studied by an experimental-numerical approach, obtaining ballistic limit velocity and critical perforation energy of each sandwich configuration, subject to impact of spherical steel projectile in the velocity range 70–170 m/s. Zhang et al. [43] performed quasi-static perforation, and ballistic impact tests for studying the influences of impact velocity (50–220 m/s), thickness of facesheet, core density, shape of the projectile head (blunt/conical/semispherical heads). The dynamic energy absorption of the sandwich panel was examined and the ballistic limit was evaluated. Rayhan et al. [44] adopted a numerical approach for investigating the improvement of energy absorption and ballistic limit of different hexagonal honeycombs (reinforced and not) under high-velocity blunt projectile impacts. Khaire et al. [45] analyzed by numerical-experimental investigation the ballistic resistance, deformation, failure mode and energy dissipation of sandwich panel subject to medium-velocity impacts (10–145 m/s) of conical-nosed projectile. The intensification of numerical simulations has also allowed to diversify the investigations along various directions, considering applications with curved panels [46], or combination of different types of impact [47].

Despite the variety of studies developed in relation to the high-velocity impact characterization of aluminum alloy honeycomb sandwich panels, the investigation as a whole is limited to core thicknesses not exceeding 25 mm. This involves narrowing the research area to a field in which the dissipation of kinetic energy attributable to the panel core tends to be secondary, if not negligible, compared to that associated with the facesheets; and this occurs regardless of the geometric properties of the honeycomb core (cell size, wall thickness), as clearly highlighted by several authors [42,48]. Furthermore, the effect of the honeycomb core on the structural response of impacted sandwiches, expressed by the impact force transmitted to the panel during the perforation, does not appear to have been specifically treated.

This paper reports a theoretical-experimental investigation aimed at characterizing the penetration behavior and ballistic limit, the energy absorption capabilities, and the impact force attenuation effect of an aluminum alloy sandwich panel, consisting of two facesheets delimiting a honeycomb core 50 mm thick, under normal impact by spherical projectiles.

The advantage of studying the behavior of a panel with a core of this thickness is twofold. On the one hand, the high honeycomb/facesheet thickness ratio tends to achieve a complete decoupling between the deformation and fracture mechanisms attributable to the main phases that can be distinguished during the perforation of the three elements constituting the sandwich panel (first facesheet, honeycomb core, second facesheet). This particular condition will allow a more rigorous application of the analytical model adopted. Secondly, it is possible to more accurately evaluate the contributions to the kinetic energy dissipation and transmitted impact force attenuation attributable to the honeycomb core subjected to perforation, and the conditions under which these contributions can vary significantly, directly influencing the overall response of the panel to ballistic impact.

The analytical model used to estimate the ballistic limit has been developed according to the energy conservation-based approach applied to sandwich panels [38–40]. This approach allows to evaluate in detail the effect of dissipation mechanisms encountered by the projectile through the three elements constituting the sandwich panel, while also considering the interactions between each facesheet and the honeycomb.

The experimental investigation has been conducted both under static and high-velocity impact conditions (150–250 m/s). In the first case the quasi-static out-of-plane compressive behavior of the sandwich panel has been characterized, defining the main axial crushing properties. The dynamic impact tests have been aimed at determining the ballistic limit, absorbed energy and impact forces.

The main novelties of the investigation can be identified as follows.

- What is proposed is an integrated theoretical-experimental model, since the experimental investigation is not only used to validate the analytical model, but also to calibrate it with reference to some crucial issues. The energy dissipation terms that govern the energy balance equations at the base of the ballistic limit calculation, depend on the modes in which plastic deformations and fractures of the individual panel components occur, also taking into account their interactions. For this reason, their formulation is defined for the specific case analyzed, based on the observation of the deformation and failure morphologies due to panel perforation, revealed by sectioning the specimens subjected to the experimental tests. The experimental results, obtained for both static and ballistic behavior analysis of the panel, are used to guide the assumption for the average flow stress of the materials, that is the mechanical property expressing their plastic behavior during the penetration process, and is a key factor in the analytical calculation of the facesheet-related dissipation terms and those involving the honeycomb core. In this way it is possible to obtain a theoretical evaluation of the ballistic limit based on assumptions in estimating the average flow stress values that are consistent with the experimental indications, in order to overcome the intrinsic uncertainty problem related to its assessment. With these premises, the calculation model can be adapted to the specific application being investigated, making it widely generalizable.

- The combined effects of the honeycomb core on energy absorption and transmission of the impact force are focused in both experimental investigation and theoretical calculation. This allows an accurate characterization of the honeycomb core's influence on the structural behavior under penetration, taking into account on the one hand its negligible effect on the projectile's velocity loss and overall energy absorption, on the other hand the remarkable influence on the force transmitted during the impact.
- The proposed analytical model, experimentally calibrated and validated, allows for the development of novel predictive analyses of the panel's behavior in relation to the energy dissipation capacity, and the attenuation of impact forces, by varying the main geometric parameters that characterize the honeycomb (whole thickness and relative wall thickness of the cells), and the ballistic condition (primarily the mass of the projectile). With this approach it is therefore possible to investigate the potential of the honeycomb core as an effective element for dissipating the kinetic energy of the projectile, and as attenuator for impact-induced load waves through the sandwich, so to define the actual role in the overall penetration behavior, and the margins for its improvement.

2. Materials and methods

2.1. Sandwich panel

A large commercial sandwich panel (sizes 1250 × 2550 mm^2) with honeycomb core was used for the experimental tests (Fig. 1a). This panel consists of two facesheets of AA 5032 alloy (each with $h = 1$ mm thickness) and a honeycomb core of AA 3003 alloy with $H = 50$ mm thickness. Fig. 1b shows the panel in top view and cross-section.

The specimens were cut from the panel using a miter saw with a special alumina cutting disc, resulting in nearly in-plane square samples with overall thickness of 52 mm, unchanged from the initial manufacturing thickness (Fig. 1c). The basic technical data sheet provided by the manufacturer is reported in Table 1.

Geometrical features of the elemental honeycomb cell have been measured and are highlighted in Fig. 2. The primitive geometry of the hexagonal honeycomb was characterized through stereomicroscopic observations of a number of cells, which appeared to exhibit minimal internal defects. The hexagonal cells have four sides 4.6 mm long and two 2.9 mm long, angled at approximately 45° (Fig. 2a). The wall thickness, measured on a micrograph obtained with an optical microscope, is approximately equal to 0.05 mm, as shown in Fig. 2b.

2.2. Static compression test

Compression tests were performed using a universal testing machine (MTS Insight 50 kN) equipped with suitable support that allows the specimens characterization under pure normal stress. Tests were carried out on square specimens with in-plane dimensions of 85 mm x 85 mm at constant crosshead speed (5 mm/min) according to the ASTM C365/C365M-22 standard, until their densification at the maximum load was allowed by the testing machine. The in-plane dimensions have been

Table 1
Honeycomb technical features.

Alveolar diameter (nominal) [mm]	≈ 9
Density [kg/m^3]	≈ 39 - 40
Stabilized compressive strength [MPa]	1.40 - 1.95
Young modulus E [MPa]	68,000 - 70,000
Shear modulus G [MPa]	20,000 - 22,000

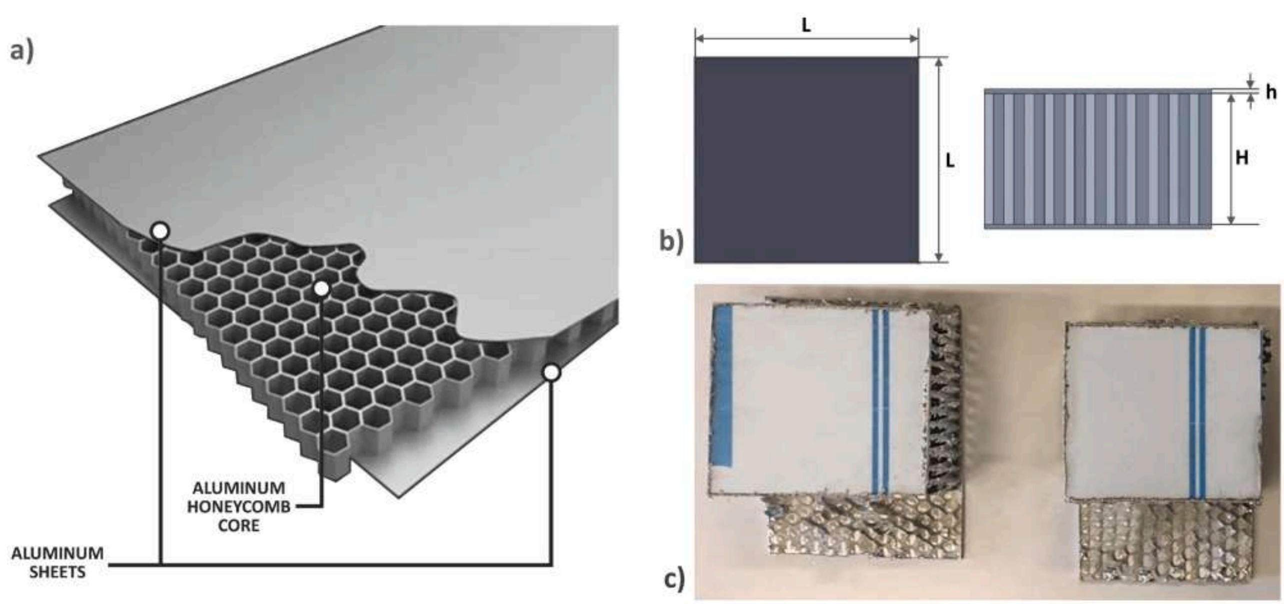

Fig. 1. Sandwich panel with honeycomb core: a) Typical Al honeycomb sandwich structure; b) Dimensions of the sandwich panel; c) Sandwich specimens obtained from the as-received panel.

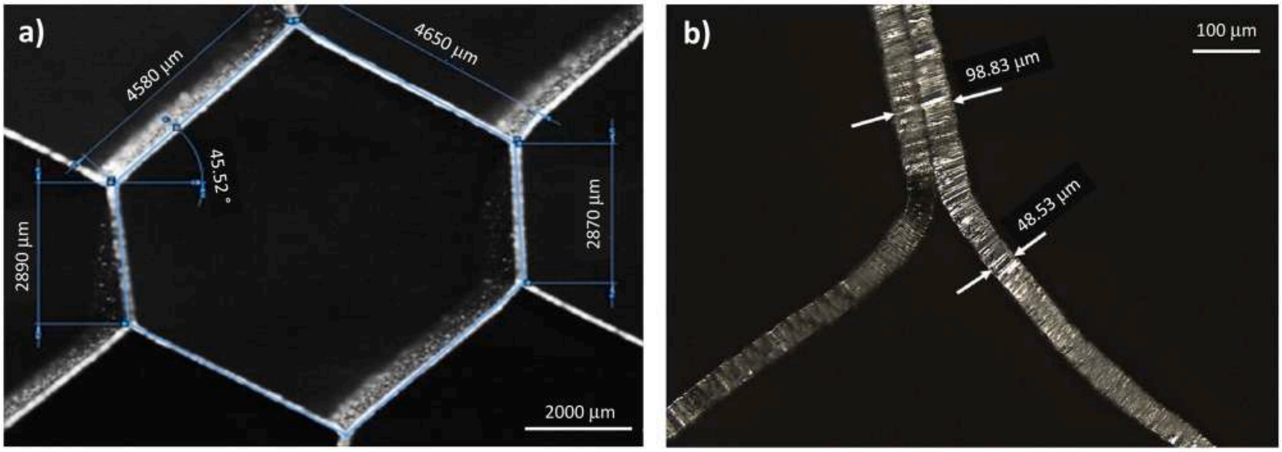

Fig. 2. Geometrical features of honeycomb cell: a) Stereomicroscope micrograph with hexagonal cell measurements; b) Optical microscope micrograph with wall thickness measurements [49].

selected according to the maximum load of the compression machine (50 kN).

Load and crosshead displacement were acquired throughout the test at a sampling rate of 10 Hz. Stress values were obtained by dividing the measured load by the cross-sectional area, while strain values by dividing the crosshead displacement by the initial height of the specimen. The measured engineering properties are listed in Table 2.

In the table the subscript "pk" is referred to the initial peak stress (maximum stress), while the subscript "m" is referred to the plateau stress, calculated as the average stress value from 0.8% to 80% strain.

The specific absorbed energy is calculated as

$$U^{*} = v\int_{0}^{\varepsilon_d^{*}} \sigma d\varepsilon \tag{1}$$

where $v = 0.018\ m^3/kg$ is the specific volume of the panel, derived from the technical specification of the producer (56 kg/m^3 density), and ε_d^{*} is the strain corresponding to the maximum efficiency.

2.3. Ballistic test

Coupons of the above panels were cut in square specimens with 120 mm x 120 mm in-plane dimensions for the ballistic tests, carried out on a single-stage gas gun equipment developed at the University of Catania, shown in Fig. 3. It is based on a 35 mm bore - 5.5 m long barrel, with a 2.2 m long reservoir made of the same pipe for oleodynamic applications used for the barrel. The gas adopted is nitrogen, compressed by a booster into the reservoir, and a manually-operated ball valve is inserted between the reservoir and the barrel to trigger the tests.

The muzzle is encased into a cubic, 0.5 m edges, containment chamber made of 12 mm thick mild steel, with transparent polycarbonate windows on its left, right and upper faces, to allow front-back-side lighting and video recordings.

The containment chamber (Fig. 4a) is divided in two sub-chambers by a divertor-and-diaphragm system for splitting the sabot in two halves, diverting them sideway and capturing their fragments into the first sub-chamber as them impact on the diaphragm, while leaving the projectile to pass into the second sub-chamber through a properly sized hole.

Table 2
Engineering properties.

σ_{pk}^{*}	Peak stress
σ_{m}^{*}	Plateau stress
η_{max}^{*}	Energy absorption efficiency
ε_{d}^{*}	ε^{*} corresponding to η_{max}^{*}
U^{*}	Specific absorbed energy

The specimens used for the ballistic tests were placed on two box-shaped supports bolted to a rigid plate. Duct tape was used to keep the specimens in the correct position during the tests. A Phantom V711 high-speed camera completes the gas-gun equipment (Fig. 4b), allowing optical measurements of the projectile speed before and, in case of full perforation, after impact with the tested coupons.

The limited in-plane dimensions of square specimens (120 mm x 120 mm) were selected in order to isolate the intrinsic mechanical behavior of the sandwich, decoupling it from global deformation mechanisms of the panel, which would affect the characterization by making it dependent on the in-plane extension of the specimens. At the same time, the chosen dimensions are sufficient to allow the full development of local deformations, with particular regard to those of the rear facesheet, on which the honeycomb core's ability to absorb energy is highly dependent. This was confirmed by the observation of impacted specimens subject to complete perforation, sectioned through the projectile trajectory (some of these sectioned specimens will be reported and commented in Section 3.2).

Beyond visual observation, the adequacy of the dimensions chosen, in relation to the extension of the local deformation area, was verified by specific conditions defined by Skvortsov et al. [39], based on the comparison between the time taken to cross the panel, and the propagation speed of shear and bending waves from the impact epicentre to the panel edges.

The sabot is designed and manufactured by 3D printing, to propel spherical projectiles into the 35 mm barrel, with a purposefully optimized shape suitable for separating from the projectile and splitting in two halves in the first sub-chamber, preventing-limiting its fragments from passing through the hole of the retaining diaphragm together with the projectile.

Spherical high-hardness steel projectiles with 8 mm diameter and 2.09 g mass were used (AISI 52100 low-alloy chromium martensitic steel, 7800 Kg/m^3 density, 2030 MPa yield strength, 60 - 66 HRC hardness); 6 mm steel spheres were also tested initially as candidate for projectiles, but the kinetic energy they acquired at the achievable speeds was not sufficient to pierce the facesheets of the sandwich panels investigated. Due to their superior yield strength relative to the aluminum facesheets and the honeycomb core, the projectiles can be considered infinitely rigid. This assumption is supported by post-impact observations, which showed that the spheres remained undeformed and devoid of surface scratches.

Non-spherical and nose-shaped projectiles were not used for the

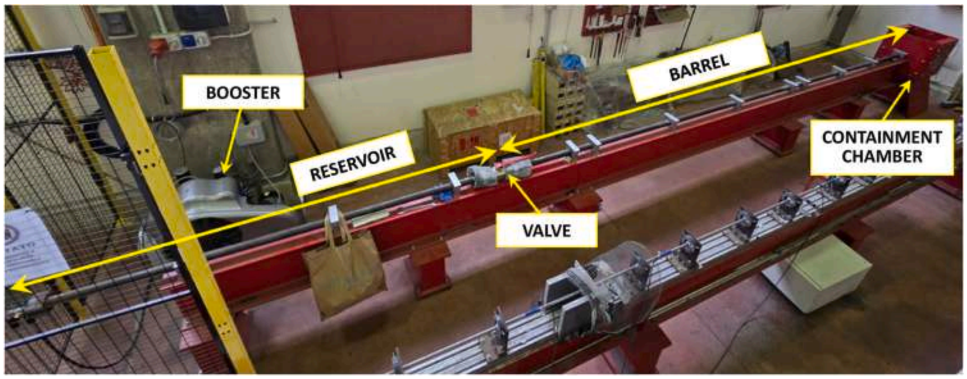

Fig. 3. Gas gun equipment.

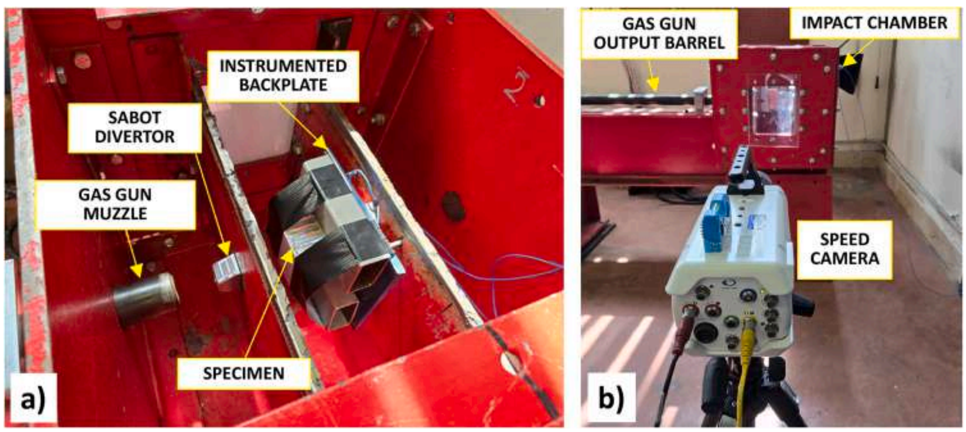

Fig. 4. Experimental setup: a) Instrumented impact chamber; b) Gas gun output barrel, impact chamber and speed camera.

present study to facilitate experimental repeatability. With such geometries, even minor misalignments at the moment of impact can lead to significant discrepancies in the results.

Fig. 5 shows the sabot, with the projectile inserted in its seat. The assembly sabot-projectile is inserted inside into the barrel of the gas gun, immediately downstream of the closed ball valve. Nitrogen is compressed in the reservoir up to the desired pressure, then the valve is manually opened to accelerate the sabot to the required velocity. The “reasonably-fast” manual operation of the valve is proved to ensure repeatable projectile speeds at each given pressure, whereas purposeful graduality in manually opening the valve determines reductions of the projectile speed for the same pressure.

After the sabot-projectile assembly exits the nozzle and travels in the first sub-chamber of the containment system, it encounters a specially shaped component named divertor, designed to split and break in two halves the adequately pre-cut sabot and diverting such two halves to impact against a rigid diaphragm, where the sabot halves break in fragments, allowing the projectile alone to pass through an hole in the diaphragm and keep running at the desired speed in the second sub-chamber and toward the target specimen.

Fig. 6 shows a representative image acquired by the speed camera during a test. The dark area at the center of the image is the silhouette of the side view of the aluminum sandwich specimen (silhouette width is the coupon thickness). The projectile travels from left to right in the image; therefore, the portion of the clear background visible on the left side of the specimen corresponds to the region crossed in free flight

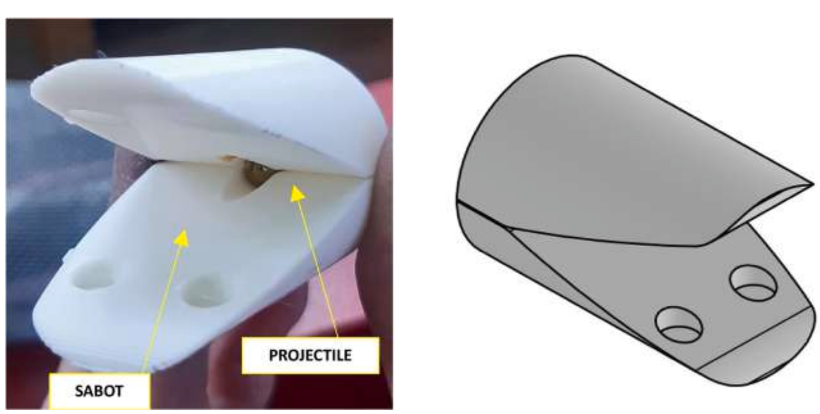

Fig. 5. Sabot with spherical projectile.

Fig. 6. Representative image from high speed video, with pre-impact and post-perforation free flight lengths.

before impacting the specimen, while the background portion to the right corresponds to the region eventually traveled after passing through the specimen, in case the projectile manages to completely perforate the coupon.

The free flight speed before impact V_{imp} and the residual velocity after complete perforation V_{res} are calculated by dividing the known flight distances by the corresponding crossing times, measured by the high-speed videos. The above speeds allow to determine the characteristic curve V_{res} vs. V_{imp} for the tested sandwich panel and its ballistic limit, i.e., the maximum projectile velocity that does not result in full perforation of the specimen.

2.4. Theoretical model

The analytical model used to estimate the ballistic limit has been developed according to the energy conservation-based approach, widely used for modeling the ballistic behavior of solid plates, cellular structures, and their combination in sandwich structures. In this last case, the perforation process is modelled according to sequential stages, related to the external layers and the core considered individually, also modelling the interactions between them [38–40]. This approach turns out to be particularly suitable for these purposes: in fact, it allows to include in the analysis, in as much detail as possible, the dissipation mechanisms encountered by the projectile through the three elements constituting the sandwich panel, while also considering the interactions between each facesheet and the honeycomb.

With this premise, a three-stage perforation model is defined (Fig. 7):

- Stage 1 refers to the phase between the impact of the projectile on the first facesheet and the completion of its penetration by the projectile. At this stage the focus is on the facesheet, but its interaction with the honeycomb core during the deformation mechanism must also be taken into account.
- Stage 2 includes the phase of complete honeycomb perforation, up to the impact of the projectile with the second facesheet.
- Stage 3 describes the perforation of the second facesheet, also taking into account the interaction with the honeycomb core due to the adhesive bonding between the two elements.

This modelling of the panel perforation process assumes complete decoupling between the deformation and fracture mechanisms attributable to the three stages. This requires that the honeycomb thickness is substantially greater than the facesheet thickness. Under this condition it can be assumed that a local crushing of the honeycomb during deformation of the first facesheet is limited and confined to a region adjacent to the latter, where the densification of the honeycomb is averted. Consequently, the second facesheet is not sensitive to the deformation of the first one. It remains substantially undeformed even during perforation of the honeycomb, unless densifications of the walls arise in the final stretch of perforation; in this case, however, any densification is confined close to the second facesheet, at a penetration depth into the cellular structure estimated to be between 75% and 84% of its original thickness [28].

The ballistic limit can be calculated on the basis of the energy balances that correlate the kinetic and dissipation terms corresponding to each stage, being equal to the velocity at which the projectile impacts the first facesheet when the residual velocity after perforation of the second facesheet is zero.

With these premises, and assuming for the input and output speeds of the projectile at each stage the nomenclature shown in Fig. 7, for a generalized formulation of the set of energy balances it is considered that:

- each perforation stage can produce a plug of mass m_{pl} that remains attached to the projectile (with mass m_p), assuming its velocity, corresponding to the stage output;

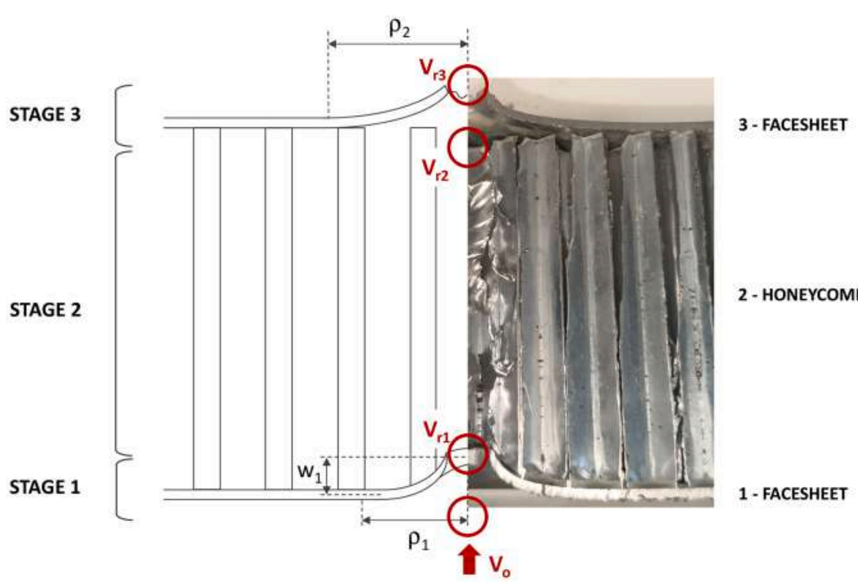

Fig. 7. Reference scheme for the three-stage perforation model.

- the energy dissipation terms are distinguished into plastic work (W_p), fracture work (W_f), and work dissipated due to the interaction between the facesheet and the core (W_i).

The energy balance equations for the three stages can therefore be defined as follows:

$$\frac{1}{2}m_p V_o^2 = W_{p1} + W_{f1} + W_{i12} + \frac{1}{2}(m_p + m_{pl1})V_{r1}^2 \tag{2}$$

$$\frac{1}{2}(m_p + m_{pl1})V_{r1}^2 = W_{p2} + \frac{1}{2}(m_p + m_{pl1} + m_{pl2})V_{r2}^2 \tag{3}$$

$$\frac{1}{2}(m_p + m_{pl1} + m_{pl2})V_{r2}^2 = W_{p3} + W_{f3} + W_{i23} + \frac{1}{2}(m_p + m_{pl1} + m_{pl2} + m_{pl3})V_{r3}^2 \tag{4}$$

where the terms m_{pl}, W_p, W_f, W_i refer to the corresponding panel components identified according to the numbering in Fig. 7 (for W_i the subscript numbers refer to the two interacting components). In Eq. (3) the dissipative effect due to the perforation on the honeycomb core is expressed just by a generic term of practical work, omitting an explicit term of fracture work, which would not be clearly associable with the collapse modalities of the honeycomb during the penetration of the projectile (described below).

Being the ballistic limit $V_{bl} = V_o$ when the residual velocity at the end of the whole panel perforation is zero, its value can be calculated using Eqs. (2–4) backwards, starting from Eq. (4) where $V_{r3} = 0$ is set.

The detailed development of the analytical model requires a series of information that cannot always be predefined or accurately predicted. The energy dissipation terms in Eqs. (2–4) depend on the modes in which plastic deformations and fractures of the individual panel components occur, also taking into account their interactions. While some of these modes can be predefined with reasonable reliability, others depend on the combination of material properties, geometric parameters of the components, and ballistic conditions. For this reason, the formulation of the energy dissipation terms will be defined later for the specific case analyzed (Section 3.3), based on the observation of the deformation and failure morphologies due to panel perforation, revealed by sectioning the specimens subjected to the experimental tests.

The experimental observation of the perforation effects on the tested specimens will also be used to measure the geometric parameters reported in Fig. 7 (ρ_1, ρ_2, w_1), which will be used in the development of the analytical calculation.

Finally, the experimental results, obtained for both static and ballistic behavior analysis of the panel, will also be used to calibrate the assessment of material's flow stress. As will be seen in the application of the model, flow stress is the key mechanical property for the analytical calculation of both the facesheet-related dissipation terms and those involving the honeycomb core. At the same time, since it must be understood as an average flow stress value, its assessment is subject to a wide margin of uncertainty due to the variety of conventional definitions proposed in the literature in the specific field of ballistic characterization.

In light of these considerations, the proposed approach should be considered as an integrated theoretical-experimental method for the ballistic characterization of the sandwich panel, in which the analytical modelling is both calibrated and validated by experimental results, so that it can be adapted to the specific application being investigated, making the model widely generalizable.

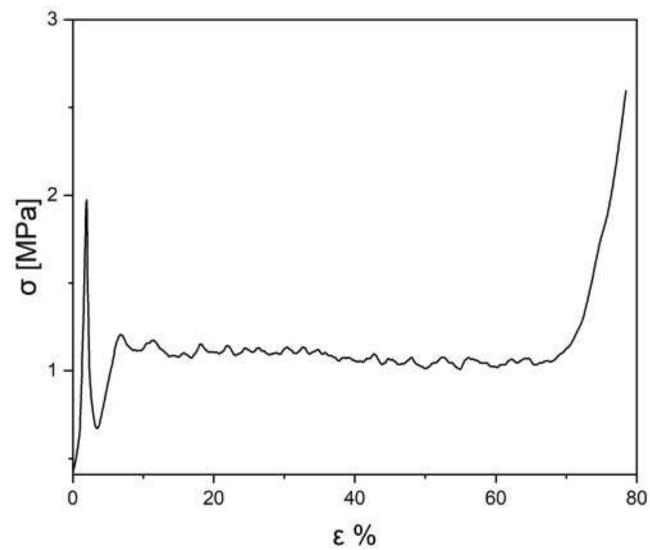

Fig. 8. Stress-strain graph in quasi-static compression test.

3. Results and discussion

3.1. Static compression test

A representative stress-strain diagram, obtained with static compression tests under pure normal out-of-plane stress, is shown in Fig. 8. This curve exhibits the stages of simple compression typical of honeycomb panels [50], which can be identified as follows:

- Pseudo-elastic phase until the peak stress is reached, in which the stress increases almost linearly with the strain. It culminates with elastic instability and plastic collapse in correspondence of the peak stress. Once the peak is passed, the stress reaches a local minimum, due to the onset of the first “folds” from instability in the plastic regime [51].
- Plateau phase, where stress remains nearly constant for a large stage of deformation as the strain increases, and numerous stress oscillations are visible. They are characteristic of the genesis of subsequent instability lobes on the cell walls, with high energy absorption, making the honeycomb panel particularly suitable for applications requiring excellent impact resistance.
- Final phase, starting at the end of the plateau when no more deformation is possible on the cell walls. It is due to the densification of the honeycomb collapsed cells, which hinders further deformation and leads to a sharp increase in stress.

In order to assess the repeatability of the deformation process, four tests were performed under the same conditions on specimens cut from the honeycomb panel. Densification onset was determined by 3% slope rule. Table 3 summarizes the mean values and the standard deviations of the parameters listed in Table 2.

3.2. Ballistic test

The ballistic tests were performed at impact speeds between 150 and 250 m/s, acquiring high-speed video with frame rate of 129,000 fps and image resolution of 590 × 80 pixels.

Table 3
Results for normal compression tests on honeycomb.

σ^*_{pk} [MPa]	σ^*_m [MPa]	η^*_{max}	ε^*_d	U^* [J /dm^3]
1.96 ± 0.29	0.93 ± 0.10	0.62 ± 0.12	0.65 ± 0.13	0.60 ± 0.07

The total energy delivered by the equipment for propelling the 32 g sabot and the 2.09 g projectile exceeded 1000 J.

The time t_{in}, required to the projectile for traveling from the rear end of the divertor to the front face of the impacted coupon, is obtained from the proper frames of the acquired video as in Fig. 9; similar considerations apply to the time t_{out} required to the projectile for traveling from the rear side of the pierced specimen to the fixed endplate with force sensors, placed at the rear end of the containment chamber.

The ratio of the above flight distances to the corresponding flight times delivers, for each test, the impact speed V_{imp} and the residual speed V_{res} (the latter only in case of complete perforation), necessary to identify the ballistic limit of the panels. At impact speed of 250 m/s and image acquisition rate of 129,000 fps, the resolution of the optical speed measurement corresponding to the interframe time is within 3%.

The crossing time, required to the projectile for traveling through the specimens and either passing through or being trapped into the second facesheet, corresponds to the impact duration (while the projectile decelerates and transfers impact force to the specimen); it is also measured by frames count.

The ratio of projectile speed change through impact to the impact duration time or crossing time T_{cr}, delivers the average (negative) acceleration A_{ng} of the projectile and the inertia force it is subjected to, which is transmitted to the sandwich as impact force F_{imp}. It is worth noting that the effective acceleration and load histories during the impact are all but constant, with local force peaks likely exceeding the time-averaged value; however, the averaged impact forces are a good comparative parameter, reported in Table 4 together with the impact and residual velocities, and the absorbed kinetic energy AE. Such data are also plotted in Figs. 10 and 11.

Two tests on couples of facesheets-only specimens are also performed, where the honeycomb is removed from the panel coupons and the two facesheets alone, positioned in mutual contact, are impacted.

The input and output speeds calculated for each test are plotted in Fig. 10, where the dots refer to the complete sandwich specimens and the hollow squares refer to the facesheets-only specimens.

The two facesheets-only tests perfectly replicated the outcome of the corresponding tests of complete sandwich specimens, evidencing that the honeycomb plays a secondary role in the impact energy absorption for the sandwich coupons adopted in this study. It is worth noting that this outcome might not be trivially extendable to larger sandwich specimens and structures, because the greater flexural compliance and the lower stiffening effect of the supporting structure on larger plates might allow the honeycomb to better contribute to the absorption of impact energy.

The discrete experimental points in Fig. 10 are finally approximated according to the Recht–Ipson model [37], which in its generalized form is widely used to obtain the ballistic limit by fitting experimental data, both in the case of solid plates [52,53] and open cellular structures such as honeycombs [32]:

$$V_{res} = a \cdot \left(V_{imp}^{p} - V_{bl}^{p} \right)^{1/p} \tag{5}$$

where a and p are model parameters and V_{bl} is the ballistic limit. The parameter values found for fitting the experimental campaign are $a = 1$, $p = 1.70$ and $V_{bl} = 195$ m/s, respectively. The hardened steel projectile undergoes negligible or no plastic strain, and no plugging was observed after complete perforation, both features fully complying with the value $a = 1$ found for approximating the experimental data in Fig. 10.

The data fitting has been extended in order to outline the range of variation of the ballistic limit, considering the variation of the experimental data. The dashed lines reported in the same Fig. 10 represent the extreme interpolations of the experimental data obtained by fitting the same model (5), which correspond to minimum and maximum values of

Table 4
Impact and residual velocities, absorbed energy, crossing times and impact forces.

Test	V_{imp} [m/s]	V_{res} [m/s]	AE [J]	T_{cr} [μs]	A_{ng} [m/s^2]	F_{imp} [kN]
6	238.15	96.12	49.64	279.07	5.09E+05	1.063
7	221.14	74.27	45.36	325.58	4.51E+05	0.943
8	158.77	-	-	573.64	2.77E+05	0.710
9	206.40	26.50	43.81	356.59	5.05E+05	1.054
10	182.12	-	-	418.60	4.35E+05	0.909
11	187.64	-	-	356.59	5.26E+05	1.100
12	206.40	60.52	40.71	333.33	4.38E+05	0.915
13	176.91	-	-	441.86	4.00E+05	0.837
14	167.35	-	-	465.12	3.60E+05	0.752
15	176.91	-	-	426.36	4.15E+05	0.867
16	187.64	-	-	379.84	4.94E+05	1.032
17	221.14	83.08	43.91	286.82	4.81E+05	1.006
18	221.14	90.78	42.52	286.82	4.55E+05	0.950
19	221.14	104.30	39.76	279.07	4.19E+05	0.875
21 (fs-only)	186.83	-	-	46.51	4.02E+06	8.395
22 (fs-only)	223.88	90.29	43.88	25.13	5.32E+06	11.112

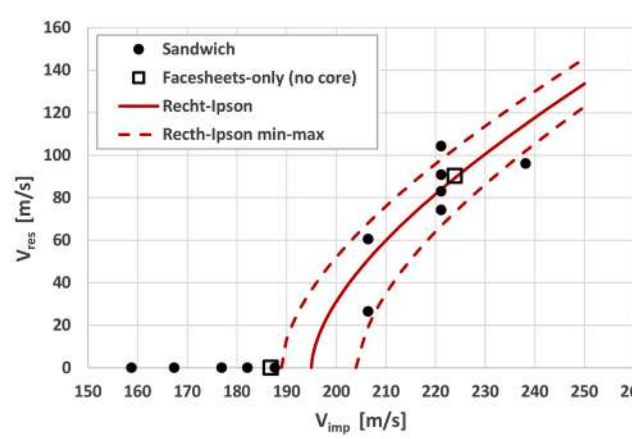

Fig. 10. Results of the ballistic tests on sandwich and facesheets-only specimens.

Fig. 9. Extracted frames for free-flight durations measurements.

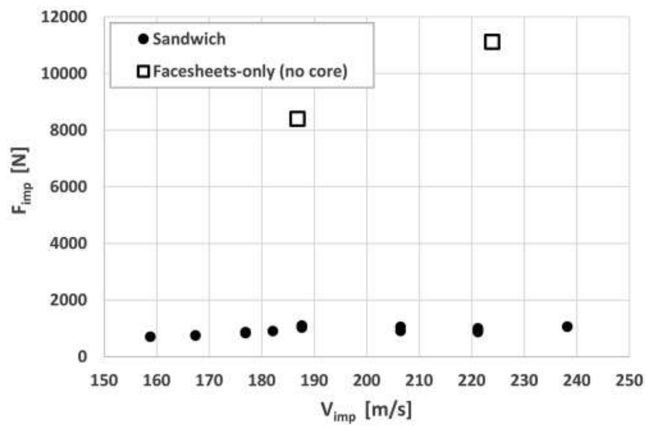

Fig. 11. Time-averaged impact forces on sandwich and facesheets-only specimens.

the ballistic limit equal to $V_{bl\_min} = 189$ m/s and $V_{bl\_max} = 204.5$ m/s (obtained for $p = 1.75$ and $p = 1.72$, respectively, and $a = 1$ in both cases).

The time-averaged impact forces F_{imp}, plotted in Fig. 11 from data in Table 4, evidence a large difference between sandwich panels and facesheets-only coupons, as the forces on the latter ones are roughly ten times greater than those on the former. This is easily explained since comparable speed decreases for both types of specimens are achieved in roughly ten times shorter crossing times for the thinner facesheets-only coupons, than for the thicker complete sandwich panels.

The overall information delivered by Figs. 10 and 11 is that the honeycomb contributes only to a limited extent in dissipating the kinetic energy of the projectile (the speed reductions after impact are comparable for both sandwich and facesheets-only coupons), but it is really efficient in distributing such speed change over much longer times, which leads to lower acceleration and impact forces.

In other words, while the role of the honeycomb core is negligible in terms of projectile speed reduction and energy absorption, its influence turned out to be remarkable when considering the transmitted force. This behaviour is attributed to the core's ability to delay stress wave propagation: the load wave transmitted through the sandwich panel is significantly longer in duration and lower in intensity compared to that observed in the facesheets-only configuration. Essentially, the core has proved to be highly efficient in mitigating the traveling load wave, despite being substantially ineffective in decelerating or arresting the projectile.

Specimens from ballistic tests have been then sectioned by planes containing the projectile motion axis, in order to analyze the features of the failure mechanisms (Fig. 12).

The images of impacted specimens sectioned through the projectile trajectory show that the edges of the coupons for impact tests were found to be longer than twice the locally deformed crater of impact on the front and the rear facesheets, which ensure that the local plastic strains involved in the impact/damage process are not affected by the close proximity of edges and support effects.

The same images clearly evidence also the effects of the interaction between facesheets and honeycomb cores. In all cases the honeycomb is locally crushed just behind the first facesheet, over a circular area roughly 9 times greater than the projectile itself (corresponding to a radial extent of 3 times the projectile diameter). Even in cases of perforation of the first facesheet only, in which the projectile impacted the second facesheet without perforating it, the latter is detached from the honeycomb over a larger area, as the polymeric bonding agent is teared. However both these facesheet-honeycomb interaction phenomena require limited amounts of energy, as the comparison between tests of complete sandwich and facesheets-only proved and the analytical model will verify.

The analysis and interpretation of failure mechanisms features that can be observed in Fig. 12 will be developed in Section 3.3.1.

3.3. Application and results of the theoretical model

The preliminary hypothesis according to which the thickness of the honeycomb core, with respect to the facesheets, is such as to decouple the failure mechanisms according to the three-stage approach previously assumed, is confirmed by a first observation of the specimens sectioned after the ballistic tests (Fig. 12). In this regard, in all the sectional tests it was found that:

- at Stage 1, the local crushing of the honeycomb during deformation of the first facesheet is limited to a region adjacent to the impact area;
- during Stage 2 the densification of the honeycomb does not occur;
- at Stage 3 the deformation of the second facesheet is not affected by the previous perforation of the honeycomb.

The energy dissipation terms governing Eqs. (2–4) are defined on the basis of the failure mechanisms attributable to the morphological characteristics of the deformations and fractures features detectable by

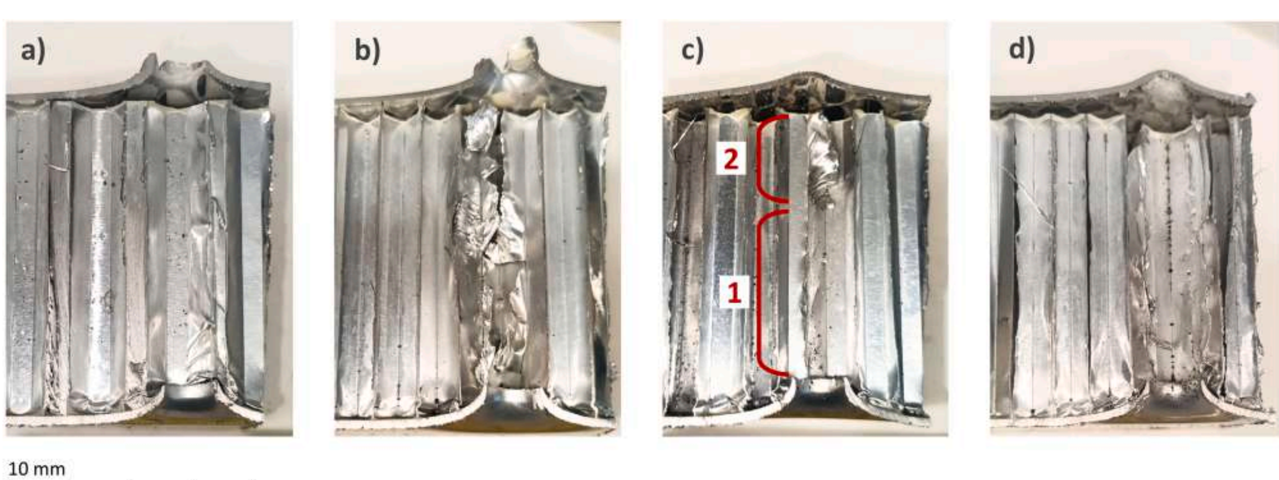

Fig. 12. Sectioned post-impact sandwich specimens: a) Test 19 (V_{imp}= 221 m/s, full penetration); b) Test 6 (V_{imp}= 238 m/s, full penetration); c) Test 14 (V_{imp}= 167 m/s, first sheet penetration); d) Test 15 (V_{imp}= 176 m/s, first sheet penetration).

observing the sectioned specimens (some more representative ones reported in Fig. 12). In this regard it should be highlighted that also the analytical formulations that will be used for the calculation of the dissipative terms have been all defined by implementing the principle of conservation of energy, in line with the assumptions of the general setting of the model.

As further assumption, all analytical formulations for the dissipative terms refer to the non-deforming projectile condition during the various indentation and penetration phases.

3.3.1. Analysis of failure morphologies and model development

The basic failure mechanisms for homogeneous metallic plates impacted by blunt cylindrical projectiles, with specific reference to aluminum targets, have been defined [54]. Shear plugging and dishing (with typical failure features due to cracks propagating along the plate thickness as a consequence of in-plane shear stresses induced by bending) generally occur for thick plates of high strength alloys. In the case of impact on thin plates, bending becomes predominant, but combined with stretching of the plate, according to an overall deformation process called dishing, which can lead to different mechanisms of final fracture, depending also on the shape of the projectile head: necking and tensile failures at the edges of indentation, with possible plug ejection; necking and tearing at the impact center with subsequent petalling; intermediate phenomena with possible combinations of these fracture mechanisms, whose onset depends not only on the thickness of the plate but also on the impact velocity, since lower velocities favor petalling, while shear plugging requires higher impact velocity [55].

As further information to be provided in defining the typology of fracture mechanisms that can be attributed to the facesheets in the case in question, it should be highlighted that experimental evidences have associated the petalling mechanism with the fracture of facesheets in aluminum sandwich with honeycomb core impacted by sharp projectiles and spheres, limiting the formation of plugs to the cases with blunt and sometimes spherically-tipped projectiles [48]. In more general terms, considering also the perforation of other metallic alloys, hemispherical and conical projectiles have proved to penetrate the target plates by pushing the material in front of the projectile aside, thus favoring ductile hole penetration and enlargement, and limiting the possibilities of shear plugging [56].

From the observation of the morphology of the first facesheet failure (Stage 1), detected experimentally by specimen sectioning (Fig. 12), the interaction between facesheet deformation and crushing of the adjacent honeycomb core is evident. This second element is effectively subjected to compression and acts as a support that stiffens the first one while it is subject to stretching and bending, and excludes the onset of a pure dishing mechanism.

As regards the final perforation of the facesheet, both from the hole cross-section and from the regularity of its cylindrical surface at the edge, the fracture can be traced back to a preliminary necking mechanism along a circumference with a radius smaller than the radius of the projectile (because of the spherical shape of the projectile used here), followed by a ductile hole formation mechanism.

To model this behavior the first facesheet can be preliminarily considered as a membrane bonded to a rigid-plastic foundation, made up of the honeycomb core, which contributes to the deformation with localized crushing [38]. In this way it is possible to combine in a single plastic work dissipation term $W_{p1.1} + W_{i12}$ the indentation and facesheet stretching, the honeycomb crushing, and their interaction through a single equation:

$$W_{p1.1} + W_{i12} = \frac{\pi\left(q_{cr\_d} + q_{sh\_d}\right)^2 r_p^4}{16h\sigma_{o\_fs}}\left\{\left(\frac{\rho_1}{r_p}\right)^4\left[ln\left(\frac{\rho_1}{r_p}\right)^4 - 1\right] + 1\right\} - \frac{\pi q_{sh\_d}\left(q_{cr\_d} + q_{sh\_d}\right) r_p^4}{4h\sigma_{o\_fs}}\left\{\left(\frac{\rho_1}{r_p}\right)^2\left[ln\left(\frac{\rho_1}{r_p}\right)^2 - 1\right] + 1\right\} \quad (6)$$

where r_p is the projectile radius, q_{cr_d} and q_{sh_d} are respectively the dynamic crushing and shear strength of the honeycomb, σ_{o_fs} is the flow stress of the facesheet material, h is the facesheet thickness, and ρ_1 is the radial extent of the facesheet deformation at the end of Stage 1 (see Fig. 7).

In case of tensile necking failure, the extent of the facesheet deformation ρ_1 can be calculated by [38]:

$$\rho_1 = r_p\sqrt{1 + 2\sqrt{2\varepsilon_{cr}}\,\frac{h\,\sigma_{o\_fs}}{r_p\left(q_{cr\_d} + q_{sh\_d}\right)}} \quad (7)$$

where ε_{cr} is the necking strain of the facesheet material.

The dynamic crushing strength for some Al alloys was found to be of the range 1.33–1.74 of quasi-static strength, because of more compacted plastic-folding mechanisms, inertial effect, and strain-rate effect [24]. With specific reference to AA 3003 alloy (used here for the honeycomb), a strain rate sensitivity of 30% has been found [40], therefore the dynamic crushing and shear strength of the honeycomb q_{cr_d} and q_{sh_d} can be approximated with good accuracy using a factor of 1.3 to be multiplied by the static crushing and shear strength of the honeycomb q_{cr} and q_{sh}. The latter can be calculated using the formulas proposed by Wierzbicki [23] and McFarland [22], respectively:

$$q_{cr} = 16.55\sigma_{o\_hc}\left(\frac{h_1}{D}\right)^{5/3} \quad (8)$$

$$q_{sh} = 0.667\sigma_{o\_hc}\frac{h_1}{D} \quad (9)$$

where σ_{o_hc} is the flow stress of the honeycomb material, h_1 is the wall thickness of the honeycomb, D is the minor cell size.

The first dissipation term for plastic deformation expressed by Eq. (6) was calculated by preliminarily assuming that the facesheet deformations are limited so that it can be considered as a membrane. As a consequence, the bending resistance of the facesheet was neglected. To complete the evaluation of the dissipated plastic energy, a further term $W_{p1.2}$ is added by adopting a basic formula for the calculation of bending work in the penetration of a thin plate [57]:

$$W_{p1.2} = \frac{\pi^2}{4}r_p h^2\sigma_{o\_fs} \quad (10)$$

As last dissipation term of Stage 1, the fracture work of the first facesheet W_{f1} can be calculate by the Taylor's formula for ductile hole formation modified by Woodward [57]:

$$W_{f1} = C\pi r_p^2 h\frac{\sigma_{o\_fs}}{2} \quad (11)$$

In this expression C is a shape factor that expresses the thickening at the edge of the hole (defined as the ratio between the lip extent at the edge of the hole, and the initial plate thickness h).

The perforation of the honeycomb core, which occurs during Stage 2, involves complex deformation mechanisms influenced by the location of initial contact relative to the cellular geometry [28]. This is even more true the more the diameter of the projectile tends towards the cell size, such as in the case in question, the diameter of the projectile (8 mm) being close to the average cell diameter ($D_{av} \sim 7.4$ mm). In this case two different deformation modes can be distinguished: (1) when the initial contact occurs in correspondence with the center of the cell, the walls are subject to bending, combined with tearing and delamination (Fig. 12a, d); (2) when penetration occurs at the cell walls, the deformation can be a combination of out-of-plane (axial) and in-plane crushing (or a transition from the former to the latter), accompanied by wall collapse and delamination (Fig. 12b).

The onset conditions of the two modes are not strictly distinguishable. Fig. 12c is an example of this, as it shows a transition between deformation mode 1 and mode 2, starting from a penetration depth of approximately 70% of the initial honeycomb thickness.

When deformation mode 2 occurs, the out-of-plane compression can produce local densification, and a plug is ejected with perforation. In the analyzed cases, no plug was detected, therefore the onset of densifications can also be excluded for deformation mode 2.

In any case, under these conditions, the energy dissipated in the honeycomb perforation process cannot be estimated with sufficient accuracy using the basic solutions to calculate the plastic work terms due to solely out-of-plane and in-plane crushing [28], because they were found to underestimate the actual dissipative effect, since they did not take into account other non-negligible dissipative mechanisms (tearing, fracture, and separation of cell walls).

For this reason, the dissipation term of Stage 2 has been derived from the ballistic limit of the bare honeycomb, appropriately corrected to account for the reduction in honeycomb thickness due to partial crushing that occurred during Stage 1 [38]:

$$W_{p2} = \frac{1}{2}\left(m_p + m_{pl1}\right) V_{bl_{hc}}^{'2} \tag{12}$$

with the corrected ballistic limit of the honeycomb expressed by

$$V'_{bl\_hc} = \sqrt{\frac{H - w_1}{H}}\, V_{bl\_hc} \tag{13}$$

where H is the honeycomb thickness, w_1 is the transverse deflection of the first facesheet at the end of Stage 1 (see Fig. 7), and V_{bl_hc} is the ballistic limit of the bare honeycomb. The latter can be estimated theoretically using analytical models present in the literature [32,33].

The failure features that can be observed in the second facesheet (Stage 3) are attributable to the combined plastic deformations of bending and stretching typical of the dishing mechanism (Fig. 12a and b), with necking and tearing at the impact center (evident in the cross-sections of the specimens subjected to ballistic tests that did not perforate the second facesheet, showing the deformation state before perforation, such as in Fig. 12c and d), and subsequent petalling. The latter is found to be the dominant fracture mechanism in all exit holes of the specimens subjected to complete perforation (such as in Fig. 12a), appearing also in the variant with a hint of plug formation, not ejected but folded away and attached to one of the petals (Fig. 12b). This is consistent with experimental evidences that, particularly for hemispherical-nosed projectiles, associate the petalling mechanism with lower impact velocities (how can those on the second facesheet be considered), while shear plugging requires, in addition to greater thicknesses, also higher impact velocities [55].

Based on these observations, the Stage 3 dissipation terms due to plastic and fracture works can be defined as follows:

$$W_{p3} = \frac{\pi\, r_p\, h\, \sigma_{o\_fs}}{2}\left(r_p + \pi h\right) \tag{14}$$

$$W_{f3} = 3.37\sigma_{o\_fs} h^{1.6}\left(2r_p\right)^{1.4} \tag{15}$$

being Eq. (14) the expression for the work of dishing according to Woodward and Cimpoeru [54], and Eq. (15) the energy dissipation due to petalling according to Wiezbicki [58].

Finally, regarding the interaction between honeycomb core and facesheet, also in this case it is well represented by the sectioned specimens (all cases in Fig. 12), and clearly attributable to a debonding action between the two components. The dissipation term due to debonding can be expressed by [38]:

$$W_{i23} = \tau_{s\_b} A_s \xi_s \tag{16}$$

where τ_{s_b} is the shear strength of the bonding (from the adhesive properties), A_s is the effective sliding surface between the second facesheet and the honeycomb structure, and ξ_s is the average sliding distance. The effective sliding surface A_s can be estimated by calculating the number of cells underlying the area of the circular portion of the facesheet affected by the debonding (that is $\pi\rho_2^2$, being ρ_2 the radial extent of second facesheet deformation at the end of Stage 3, reported in Fig. 7), and multiply this number by the cross-section area of the cell. The average sliding distance ξ_s can be approximated by evaluating an average value of elongation to which the points on the facesheet inner surface, along the radial extension ρ_2, were subjected after bending and stretching. Geometric parameters ρ_2 and ξ_s can be evaluated by experimental measurements on sectioned specimens.

3.3.2. Evaluation of material properties for plastic behavior

As can be observed from the set of analytical formulations defined in the previous section, in the calculation of the dissipation terms of balance Eqs. (2–4) the mechanical behavior of honeycomb and facesheet materials in the plastic field is modelled by introducing the corresponding flow stress (σ_{o_hc} and σ_{o_fs}, respectively). They must be understood as flow stress average values, which should represent "on average" the behavior of materials during the plastic deformations. By their very nature, therefore, their evaluation is subject to a wide margin of uncertainty, also due to the variety of indications present in the literature for this purpose.

Indeed, in the specific field of ballistic characterization, a wide variety of suggestions have been given for the evaluation of these two fundamental terms, often related to the specific dissipation work to be calculated, and calibrated on the corresponding experimental evidences analyzed in each investigation.

For the honeycomb material behavior in quasi-static crushing, Wierzbicki [23] discusses several alternatives for evaluating σ_{o_hc} to be used in Eqs. (8) and (9), assuming preliminarily that the flow stress value varies between yield strength σ_y and ultimate strength σ_u of the material. An expression for the average crushing strain (as a function of relative thickness of the honeycomb walls h_1/D) is proposed, to be used for obtaining the corresponding value of flow stress (from the true stress-strain relation, or directly from the true curve of the material). Alternatively, an approximate formula is defined to calculate the flow stress as a fraction of the ultimate strength $\psi\cdot\sigma_u$, where ψ is a function of the ultimate strain of the material ε_u and the relative wall thickness of the honeycomb h_1/D. As a further conclusion of the investigation, based on experimental results, a flow stress estimate of $0.7\cdot\sigma_u$ is proposed, to be used specifically for some aluminum alloys, while highlighting that for the AA 5000 series the experimental data fit better with $\sigma_{o\_hc} = \sigma_u$.

For dynamic behavior of plate materials subjected to fracture mechanism of ductile hole formation, Woodward [57] points out that in general terms it is reasonable to use an average flow stress at large strain, where the true stress-strain curve is nearly flat, but concludes his investigation assuming that the dissipated work expressed by Taylor's Formula (11) can be calculated with reliable approximation by using the flow stress value at 1.0 true strain.

To calculate the fracture work due to petalling of plates, Wierzbicki [58] indicates a specific formulation for flow stress to be used in Eq. (15), expressed as a function of σ_y, σ_u, and the exponent in the true stress-strain power law of the material.

More generally, Hoo Patt and Park [38] assume the same approximate formulation of average flow stress for all the terms used in their model, both for σ_{o_hc} and σ_{o_fs}, setting them equal to the average value between σ_y and σ_u of the corresponding material; that is an approximation often used in the field of cold working, particularly if strain hardening is limited [59].

In the application of the present model the following approximations will be considered for the average flow stress calculation:

- the average value between σ_y and σ_u [38]
- the mean integral value of a significant portion of the true curve of the material [60], assuming for the latter the part of the curve where the strain hardening tends to stabilize [57]
- the reduced value of ultimate strength as $0.7\cdot\sigma_u$ [23]

- the reduced value of ultimate strength as $\psi \cdot \sigma_u$ (where ψ is a function of the ultimate strain ε_u and the relative wall thickness of the honeycomb h_1/D) [23]

The first two can be considered for both facesheets and honeycomb (σ_{o_fc} and σ_{o_hc}) while the last two have been specifically suggested for honeycomb (σ_{o_hc} only).

To address the significant level of uncertainty due to the variety of flow stress formulations, the experimental results, obtained for both static and ballistic behavior analysis of the panel, will be used to calibrate and guide the final assumption for both honeycomb and facesheet material flow stresses. Specifically, the results of experimental investigations will be used as follow:

- the static crushing strength q_{cr} estimated experimentally ($\sigma_m{}^*$ in Section 3.1) will be used to calculate by Eq. (8) a reference value for σ_{o_hc};
- the range of variation of the ballistic limit defined by the experimental data fitting reported in Section 3.2 will be use to obtain the corresponding range of flow stress values for facesheets material σ_{o_fs}, by applying the theoretical model calculation with ballistic limit as input, and setting σ_{o_hc} equal to the value determined as specified in the previous point.

These values, derived from experimental investigations, will be compared to the corresponding values of σ_{o_hc} and σ_{o_fs} obtained from the properties of the panel materials, using the basic theoretical assumptions chosen as references, described above. In this way it will be possible to obtain a theoretical evaluation of the ballistic limit based on assumptions in estimating the average flow stress values that are consistent with the experimental indications, in order to overcome the intrinsic uncertainty problem related to this key parameter.

As a final observation, given the high-impact velocities up to 250 m/s, in general terms the effect of strain-rate sensitivity in the modelling of materials behavior should be taken into account. Specifying that the strain-rate sensitivity of aluminum alloys was proven to be limited [61], the alloy used for the honeycomb (AA 3003) has shown an appreciable sensitivity of 30% [40]. For this reason, as reported in the previous Section 3.3.1, the dynamic crushing and shear strength of the honeycomb q_{cr_d} and q_{sh_d} was approximated using a factor of 1.3 to be multiplied by the static crushing and shear strength of the honeycomb q_{cr} and q_{sh}. AA 5052 alloy, used for the facesheets, has instead proven to be substantially insensitive, showing strength enhancement under impact loading only in the case of cellular structures, attributable to inertia effect in folding process [62]. For this reason, the effect of the strain-rate on this specific material used in plate form for the facesheets has been neglected.

3.3.3. Application of the model and results

In applying the model set up in Section 2.4 and developed in Section 3.3.1, the following additional assumptions have been made.

The formulas introduced in Section 3.3.1 for the calculation of the dissipation terms mostly refer to the impact of blunt cylindrical projectiles. As already highlighted by other authors [38], in the case of spherical projectile the contact radius in facesheet impact varies during indentation and perforation, and so an average contact radius of the spherical projectile should be assumed. For this purpose, a reduction factor for the radius r_p was set as $\eta = 0.785$, obtained by evaluating the mean integral value of the radius of the hemispherical indentation cap along the longitudinal axis, that can be calculated as $\pi/4 \cdot r_p$. In this way the hemispherical indentation shape of maximum radius r_p is approximated by an equivalent cylindrical shape of radius $\eta \cdot r_p$, with the same longitudinal cross-section area.

The reduction for r_p was not applied in Eq. (11) for the calculation of the fracture work due to ductile hole formation mechanism, which refer to cylindrical-conical projectiles. In this case, the value of the shape factor C (that expresses the thickening at the edge of the hole due to enlargement) was originally defined by Taylor as $C = 2.66$, even though subsequent studies attributed to this value the underestimation of dissipation work compared to experimental results [63]. However, the C values measured along the edges of the holes in the sectioned specimens (Fig. 12), as the ratio between the extent of the lip at the edge of the hole and the initial plate thickness h, remained on average below 2, and therefore the original Taylor coefficient was considered suitable for the specific application. Even if in excess with respect to the experimentally measurable thickening, this value can compensate for the spherical shape of the projectile used in the application, considering that the hole formation work tends to increase with the nose angle of the projectile [57].

As regards the plug masses m_{pl} introduced in the generalized energy balance Eqs. (2–4), here they can be omitted. The fracture mechanisms defined for the two facesheets (short-range peripheral necking and ductile hole formation for the first, necking at the impact center and petalling for the second one), in both cases exclude the formation of plugs (also in the case of petalling with partial plug formation, such as in Fig. 12b, no kinetic contribution is attributable to the plug since it is not subject to ejection but remains attached to one of the petals). This is also an effect of the hemispherical impacting shape of the projectile on plates, which has been proved to favor ductile hole penetration and enlargement, limiting the possibilities of shear plugging [56].

In a similar way, also the perforation of bare honeycomb core by spherical projectiles does not result in plug ejection, as instead happens in the case of blunt projectiles [28]. Therefore, it is concluded that $m_{pl1} = m_{pl2} = m_{pl3} = 0$ can be set in Eqs. (2–4).

The ballistic limit of the bare honeycomb to be used in Eq. (13) has been estimated by Liaghat et al. analytical model [33], appropriate for cases where the projectile diameter is greater than the cell size, and here reformulated to highlight the term h_1/D (relative wall thickness of the honeycomb):

$$V_{bl\_hc} = \frac{1}{\sqrt{m_p}}\left[234H\sigma_{o\_hc}r_p^2\left(\frac{h_1}{D}\right)^{5/3} + 21r_pHE_{s\_hc}\left(\frac{h_1}{D}\right) + 1.35\tau_{s\_hc}r_pH^2\left(\frac{h_1}{D}\right)\right]^{0.5} \tag{17}$$

where E_{s_hc} is the fracture energy per unit area of honeycomb material, and τ_{s_hc} is its shear strength.

In the same Eq. (13), the value of the transverse deflection of the first facesheet at the end of Stage 1 (w_1 in Fig. 7) has been evaluated as the average value of experimental measures on the sectioned specimens. The same was done for geometric parameters ρ_2 and ξ_s in Eq. (16).

With the previous further assumptions, the model has been applied. In Table 5 the preliminary input data for calculation (referred to

Table 5
Preliminary input data.

Projectile		
m_p [g]	2.09	Mass
r_p [mm]	4.0	Radius
η	0.785	Reduction coefficient for radius
Facesheet		
h [mm]	1.0	Thickness
Honeycomb core		
H [mm]	50	Thickness
h_1 [mm]	0.05	Wall thickness
D [mm]	6.5	Cell size (minor inner diameter)
D_{av} [mm]	7.4	Cell size (average diameter)
Bonding		
τ_{s_b} [MPa]	23	Shear strength of the adhesive (two-component polyurethane)

projectile and panel components) have been collected.

Experimental data obtained by static and ballistic investigation (Sections 3.1 and 3.2) have been reported in Table 6. On the right side of the table the derived experimental data, for calibrating and guiding the assumption for honeycomb and facesheet material flow stress values σ_{o_hc} and σ_{o_fs} to be used in the theoretical model (according the indications in Section 3.3.2), are also reported. In the lower part of the table, the values of geometrical parameters should be understood as average values estimated through direct measurements on the specimens subjected to ballistic tests and subsequently sectioned (as in Fig. 12).

Tables 7 and 8 show the properties of the aluminum alloys constituting the honeycomb core (AA 3003) and facesheets (AA 5052), respectively. The upper part of each table shows the values of the basic properties, in the form of a range. The lower part shows the corresponding values for the average flow stress, calculated according to the selected assumptions previously specified in Section 3.3.2.

Comparing these last values for the honeycomb with the experimentally derived reference value for σ_{o_hc} reported in Table 6 (187.5 MPa), it is evident that the first approximation of Wiezbicki (σ_{o_3} in Table 7) is unsuitable for the material in question (as it had already been found also for the AA 5000 series) [23]. All the other three alternatives may instead be congruent. As regards the value of σ_{o_fs}, both alternatives (σ_{o_1} and σ_{o_2} in Table 8) provide ranges of values compatible with the experimentally-derived indications (177.0 - 226.2 MPa in Table 6).

With these preliminary indications on the admissible flow stress values for the theoretical model, a set of four conditions for material properties has been defined to develop the analytical calculation:

1. $\sigma_{o\_fs} = \sigma_{o\_1}$, $\sigma_{o\_hc} = \sigma_{o\_4}$, minimum value of the ranges for both
2. $\sigma_{o\_fs} = \sigma_{o\_1}$, $\sigma_{o\_hc} = \sigma_{o\_4}$, maximum value of the ranges for both
3. $\sigma_{o\_fs} = \sigma_{o\_1}$, $\sigma_{o\_hc} = \sigma_{o\_4}$, mean value of the ranges for both
4. σ_{o_fs} and $\sigma_{o\_hc} = \sigma_{o\_2}$ (for each one refer to the value corresponding to the specific material)

Analyzing conditions 1–3 separately allows to verify the impact of uncertainty in the basic material property data, all expressed as ranges of values (upper parts of Tables 7 and 8).

Condition 4 represents the reference constituted by the choice of the average flow stress values obtained by integration of the true curves (both for facesheet and honeycomb materials).

The results obtained applying the theoretical model, for each of the four conditions, are reported in Table 9, with the following arrangements:

- For each calculated term the corresponding equation is reported in the second column.
- For the terms previously acquired experimentally (Table 6), in addition to the theoretically calculated value, the percentage deviation from the corresponding experimental value is reported (in brackets).

Table 6
Experimental data (resulted and derived).

Static characterization			
q_{cr} [MPa]	0.93	σ_{o_hc} [MPa]	187.5
Ballistic characterization			
V_{bl} [m/s]	195.0 ($a = 1, p = 1.70$)		
$V_{bl\ min}$ [m/s]	189.0 ($a = 1, p = 1.75$)	$\sigma_{o\_fs\ min}$ [MPa]	177.0
$V_{bl\ max}$ [m/s]	204.5 ($a = 1, p = 1.72$)	$\sigma_{o\_fs\ max}$ [MPa]	226.2
Geometric parameters			
ρ_1 [mm]	19.8		
w_1 [mm]	6.0		
ρ_2 [mm]	23.9		
A_s [mm^2]	48		
ξ_s [mm]	0.5		

Table 7
Honeycomb material properties (AA 3003).

Basic mechanical properties		
σ_y [MPa]	172 - 186	Yield strength
σ_u [MPa]	179 - 200	Ultimate strength
τ_s [MPa]	95 - 102	Shear strength
ε_u	0.10 - 0.14	Ultimate strain
E_s [kJ/m^2]	14 - 16	Fracture energy per unit area
Average flow stress		
σ_{o_1} [MPa]	176 - 193	Yield-ultimate strength mean value
σ_{o_2} [MPa]	206	Mean integral value of true curve
σ_{o_3} [MPa]	125 - 140	$0.7{\cdot}\sigma_u$ (honeycomb only)
σ_{o_4} [MPa]	141 - 186	$\psi{\cdot}\sigma_u$ (honeycomb only)

Table 8
Facesheet material properties (AA 5052).

Basic mechanical properties		
σ_y [MPa]	175 - 193	Yield strength
σ_u [MPa]	196 - 228	Ultimate strength
ε_u	0.12 - 0.18	Ultimate strain
Average flow stress		
σ_{o_1} [MPa]	185 - 210	Yield-ultimate strength mean value
σ_{o_2} [MPa]	236	Mean integral value of true curve

- For each stage of the perforation process, all dissipation terms and their overall value (W_{S1}, W_{S2}, W_{S3}) are reported. Their sum, expressing the total energy dissipation in the complete perforation of the entire sandwich panel, are also reported as W_{SP}. The percentage contribution of each stage with respect to the total energy dissipation is indicated (in brackets).
- Finally, he theoretical values of the ballistic limit with the percentage deviations from the experimental value (195 m/s), and of the maximum impact force (that is, the impact force corresponding to the ballistic limit), are reported in the last rows of the table.

In all the conditions analyzed, ballistic limit values close to the experimental one are obtained (deviation within 10%). The mean values of the property ranges (condition 3) give a result fully superimposable to the experimental value (+0.8%). The results of conditions 1–3 are all within the range of minimum and maximum values of the ballistic limit corresponding to the extreme interpolations of the experimental data (189 m/s and 204.5 m/s in Table 6). Only the result corresponding to condition 4 exceeds the experimental range of values. Although it maintains a deviation from the experimental reference value (195 m/s) within 10%, it is not consistent with the results of tests 9 and 12 (Table 4), which for an impact velocity of 206.4 m/s reveal a complete perforation of the panel with residual velocities (albeit very low, therefore in conditions close to the ballistic limit).

Even all the theoretical values of the geometric parameter characterizing the deformation of the first facesheet (ρ_1) are consistent with the experimental average value (deviation within 7%). In this case, the minimum values of the property ranges (condition 1) give a result fully compliant with the experimental data (+0.6%).

The data most sensitive to the variability of the material properties is the crushing strength q_{cr}, which assumes substantially different theoretical values. However, with the exception of condition 1, the other values are quite consistent with the experimental data (0.930 MPa). Among these, the value corresponding to condition 2 is completely superimposable.

Overall, it can be concluded that, despite considering the ranges of variation in the basic mechanical property data of the materials and the different assumptions for setting the values of average flow stress, the analytical calculation results are highly consistent with the experimental results. This is particularly true for the evaluation of the ballistic limit, which can be considered fully validated within the range of 190–203 m/

Table 9
Results of theoretical calculation.

		1	2	3	4
Crushing properties					
q_{cr} [MPa]	Eq. (8)	0.699 (−24.8%)	0.924 (−0.6%)	0.799 (−14.0%)	1.027 (+10.4%)
q_{sh} [MPa]	Eq. (9)	0.723	0.956	0.827	1.062
q_{cr_d} [MPa]		0.930	1.229	1.063	1.366
q_{sh_d} [MPa]		0.961	1.271	1.099	1.412
Stage 1					
ρ_1 [mm]	Eq. (7)	19.9 (+0.6%)	18.5 (−6.6%)	19.3 (−2.7%)	18.6 (−6.1%)
$W_{p1.1} + W_{i12}$ [J]	Eq. (6)	3.776	4.107	3.955	4.631
$W_{p1.2}$ [J]	Eq. (10)	1.434	1.628	1.531	1.829
W_{f1} [J]	Eq. (11)	12.368	14.039	13.203	15.777
W_{S1} [J]		17.578 (46.5%)	19.774 (46.1%)	18.689 (46.3%)	22.239 (46.8%)
Stage 2					
V_{bl_hc} [m/s]	Eq. (17)	79.5	86.1	82.8	87.1
V'_{bl_hc} [m/s]	Eq. (13)	74.6	80.8	77.7	81.7
W_{p2} [J]	Eq. (12)	5.813	6.818	6.305	6.977
W_{S2} [J]		5.813 (15.3%)	6.818 (15.9%)	6.305 (15.6%)	6.977 (14.7%)
Stage 3					
W_{p3} [J]	Eq. (14)	5.736	6.511	6.124	7.317
W_{f3} [J]	Eq. (15)	8.171	9.275	8.723	10.423
W_{i23} [J]	Eq. (16)	0.525	0.525	0.525	0.525
W_{S3} [J]		14.432 (38.2%)	16.311 (38.0%)	15.371 (38.1%)	18.265 (38.5%)
Entire panel					
W_{SP} [J]		37.822	42.903	40.366	47.480
Ballistic limit					
V_{bl} [m/s]		190.2 (−2.5%)	202.6 (+3.9%)	196.5 (+0.8%)	213.1 (+9.3%)
Impact force					
F_{imp_max} [kN]		0.727	0.825	0.776	0.913

s defined by conditions 1–3, with a deviation from the experimental value not exceeding ±4%. Furthermore, since the only value that is not well consistent with the experimental results is the one corresponding to condition 4, it can be concluded that the most appropriate assumption on the estimation of the average flow stresses for the materials is the combination of yield-ultimate strength mean value for the facesheets, and $\psi \cdot \sigma_u$ for the honeycomb ($\sigma_{o\_fs} = \sigma_{o\_1}$ and $\sigma_{o\_hc} = \sigma_{o\_4}$, according to the nomenclature for average flow stress in Tables 7 and 8).

As regards the distribution of dissipative effects across the three stages of the perforation process, it remains substantially unchanged for all the conditions analyzed, and the contribution of the first stage is predominant compared to the other two (46–47%).

Looking at the single dissipation terms, those due to fracture mechanisms at Stages 1 and 3 are the most significant (W_{f1} and W_{f3}). It can also be observed that the interactions between the facesheets and the honeycomb give very limited dissipation contributions, which are a fraction of $W_{p1.1} + W_{i12}$ at Stage 1, and W_{i23} at Stage 3. Regarding the latter, that is the dissipation term due to debonding between second facesheet and the honeycomb, it should be noted that it is the lowest one, and it is unchanged for all the conditions analyzed. The reason is that its calculation, using Eq. (16), is independent of the material properties.

As a further observation on the overall set of dissipation terms, considering the results of conditions 1–3, i.e. those fully congruent with the experimental results on ballistic limit, an average value of 40.37 J is found for the total energy dissipations of the entire sandwich panel W_{SP}. This value is in agreement with the average value of 42.26 J for the energy absorption measured by the experimental tests 9 and 12 (Table 4), carried out in the condition closest to the ballistic limit (impact velocity of 206.4 m/s), and therefore comparable to the theoretical results in Table 9.

In substantial agreement with what was revealed by the facesheets-only tests, compared with the results of full-panel tests at the same impact velocity, the dissipative contribution of the Stage 2 is limited, although not negligible (14–16%), due to the high thickness of the honeycomb core. The effect of the honeycomb thickness on this dissipation term is evident if, using Eqs. (12), (13), and (17), the projections of W_{p2} are developed as the thickness H varies. They are reported in Fig. 13 for the four conditions analyzed, and reveal quadratic polynomial correlations, which highlights the high-potential effect of the honeycomb core thickening in terms of contribution to the overall dissipation in the panel.

This effect is even better appreciated if associated with the other geometric properties of the honeycomb. In Eq. (17) the original expression of Liaghat et al. [33] has been appropriately reformulated to highlight the role of the relative wall thickness h_1/D (an expression of the density of cellular structure). Given the same characteristics of the first facesheet (material, thickness, interaction with the honeycomb), and for similar ballistic conditions (equal mass, shape, and diameter of the projectile and a sufficiently limited range of impact velocities), it is possible to consider negligible the variation of the average value assumed for w_1. Under these conditions, and set a reference value for the average stress flow σ_{o_hc}, Eqs. (12), (13) and (17) as a whole depend only on the parameters H and h_1/D, which define geometrically the honeycomb structure, and can be used as variables to analyze the effect of its geometrical configuration on W_{p2}.

Assuming for σ_{o_hc} the condition 3 (mean values of range properties), in Fig. 14 the trends of W_{p2} are shown as the thickness H varies, for some values of h_1/D: 0.008 identifies the curve of the panel analyzed, while the other values are attributable to different configurations available for the same type of panel. Therefore, the point highlighted on the 0.008 curve represents the case analyzed, with W_{P2}= 6.305 J, which corresponds to a limited contribution of energy dissipation (15.6% of the total, as reported in Table 9, condition 3).

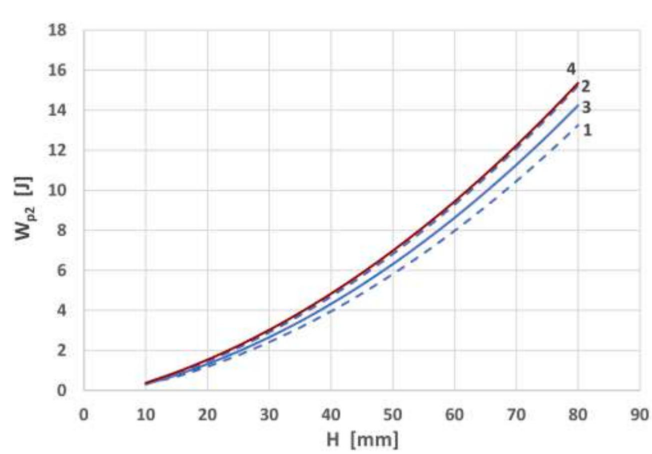

Fig. 13. Trends of honeycomb core dissipation W_{p2} as the thickness H varies (four conditions for properties of materials).

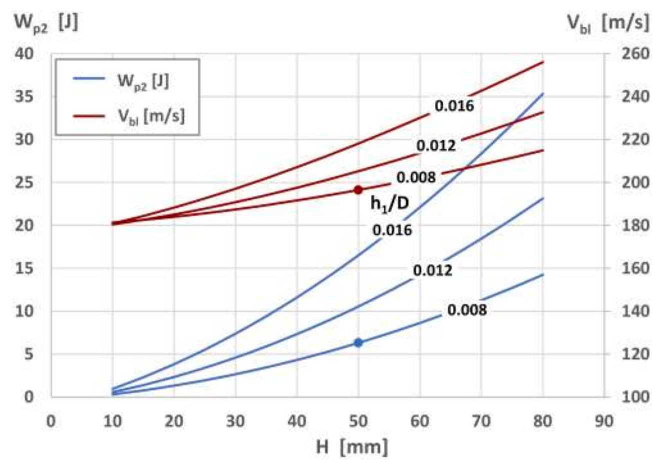

Fig. 14. Trends of honeycomb core dissipation W_{p2} and ballistic limit V_{bl} of the whole sandwich as the thickness H varies, for some values of relative wall thickness h_1/D (condition 3 for properties of materials).

It is evident that, for honeycomb structures that combine the values of H and h_1/D in different ways, more limited or vice versa much more marked dissipation effects can be obtained. Particularly, the curves in Fig. 14 confirm the conclusions of other authors for sandwich panel of the same materials and limited core thickness (10–20 mm), according to which the thickness of facesheet is the most important factor in energy dissipation, while honeycomb geometric parameters limitedly affect the overall energy absorption of the panel [42]. But for high-thickness honeycomb core, its contribution of energy dissipation increases significantly. In the case analyzed, all other conditions being equal, by combining high values of H with various levels of density parameter h_1/D, W_{p2} could exceed values of 15 J, providing the greatest dissipative effect, in the whole overview of dissipation terms.

The second set of curves reported in the same diagram of Fig. 14 describes the trend of the ballistic limit V_{bl} referred to the whole sandwich, corresponding to the same parameters H and h_1/D that characterize the geometry of the honeycomb. These parameters have effects on V_{bl} similar to those on W_{p2}, as the ballistic limit increases with the increase of the dissipation terms. The point highlighted on the 0.008 curve (for $H = 50$ mm) represents the case analyzed, with V_{bl}= 196.5 m/s (i.e. the value of the ballistic limit calculated for condition 3, as reported in Table 9).

The information obtained through the calculation model can be completed with the theoretical evaluation of the maximum impact force F_{imp_max} that the projectile can transmit to the panel during perforation, with reference to the conditions for which complete perforation occurs. Given the same properties of the projectile and the sandwich panel, and in case no plug forms during the perforation stages, F_{imp_max} value is unique for all impact velocities starting from the ballistic limit ($V_o \geq V_{bl}$); therefore, F_{imp_max} can be defined as the impact force corresponding to the ballistic limit.

Referring to the notation of the first impact and residual velocities used in the analytical modelling (V_o and V_{r3} respectively, Fig. 7), and considering the average between these two as the crossing speed of the projectile through the panel, the crossing time T_{cr} can be calculated as:

$$T_{cr} = \frac{2(2h + H)}{V_o + V_{r3}} \tag{18}$$

Since the negative acceleration of the projectile A_{ng} can be expressed by the ratio between the speed reduction ($V_o – V_{r3}$) and the crossing time T_{cr}, based on the previous premises on the evaluation of the maximum impact velocity F_{imp_max}, it can be expressed as:

$$F_{imp\_max} = \frac{m_p\left(V_o^2 - V_{r3}^2\right)}{2(2h + H)} = \frac{m_p\ V_{bl}^2}{2(2h + H)} \tag{19}$$

This equivalence is confirmed by the energy balance Eqs. (2–4), which in the absence of plugs allow to verify that ($V_o^2 – V_{r3}^2$) is equal to a function of dissipation terms and projectile mass, which is constant for any value of $V_o \geq V_{bl}$, and therefore also for V_o= V_{bl} (to which V_{r3}= 0 corresponds). This last result can be traced back to one of the characteristics of the energy conservation-based approach to the analytical modelling of ballistic behavior, which is the independence of the dissipation terms from the impact velocity [36].

The results of maximum impact forces calculation are reported in the last row of Table 9, for the four conditions analyzed. Considering also in this case the results of conditions 1–3, i.e. those fully congruent with the experimental results on ballistic limit, an average value of 0.776 kN is found for F_{imp_max}. This value is 20% lower than the average value of 0.973 kN for the impact force measured by all full-perforation experimental tests (Table 4), which are equivalent from the point of view of estimating F_{imp_max}, regardless of the first impact velocity V_{imp}. This deviation from the experimental value is attributable to the analytical model's tendency to underestimate the total energy dissipation of the entire panel, compared to the experimental result (as found previously); this translates into a consequent underestimation of A_{ng} (amplified by the quadratic relationship with the velocities), and therefore of the theoretical F_{imp_max}.

Fig. 15 shows the theoretical projections of F_{imp_max} calculated by Eq. (19) as the thickness H varies. The same diagram also shows the experimental values reported in Table 4, for only the tests in which complete perforation occurred. This allows to observe a significant consistency between the experimental data and the corresponding theoretical evaluations, even taking into account the underestimation highlighted above for the theoretical behavior of the cored sandwich.

For the coreless configuration (perforation of only the facesheet pair), it is possible to estimate significant peak impact force values, which can be strongly reduced by interposing honeycomb cores with H starting from 5–10 mm. The impact force reduction effect continues significantly as H increases, although this effect tends to saturate.

Assuming for σ_{o_hc} the condition 3 (mean values of range properties), in Fig. 16 the theoretical projections of F_{imp_max} are shown as the thickness H varies, parametrized according the projectile mass m_p (the mass values considered are those corresponding to spherical projectiles of 8, 10, 12 mm diameter) and the relative wall thickness h_1/D (the same values of h_1/D as those in Fig. 14 were considered). The point highlighted on the curve for m_p= 2.09 g and $h_1/D = 0.008$ represents the case analyzed, with F_{imp_max}= 776 N (as reported in Table 9, condition 3).

On the basis of these findings, it can first be observed that for values of H within 20 mm the attenuation trend of F_{imp_max} as H varies is not sensitive to h_1/D. However, for $H > 20$ mm the increase in h_1/D reduces

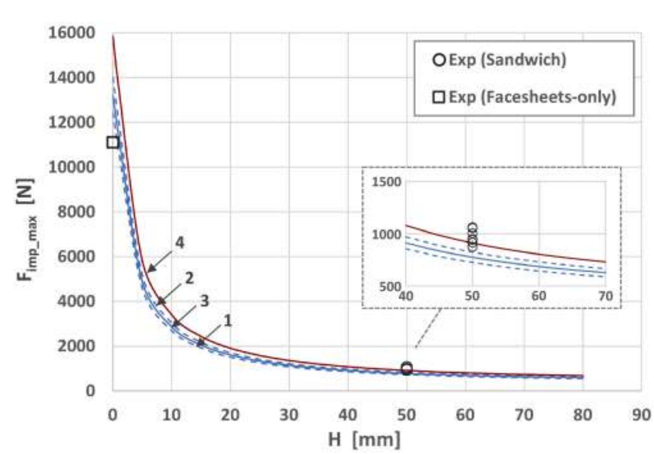

Fig. 15. Trends of the maximum impact force F_{imp_max} as the thickness H varies (four conditions for properties of materials), and corresponding experimental values from Table 4.

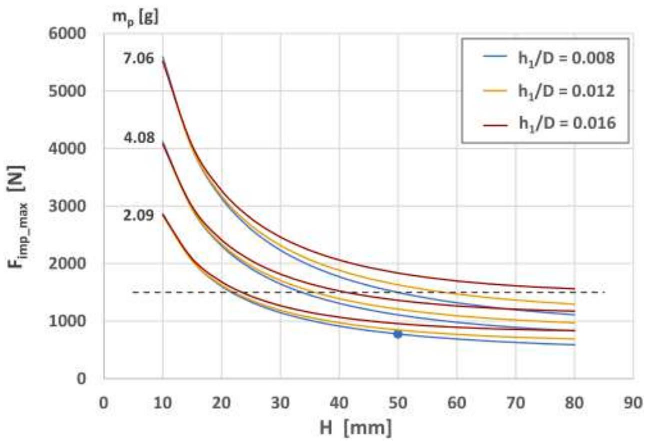

Fig. 16. Trends of the maximum impact force F_{imp_max} as the thickness H varies, parametrized according to projectile mass m_p and the relative wall thickness h_1/D (condition 3 for properties of materials).

the core's ability to attenuate F_{imp_max}. This occurs because the increase in h_1/D, with the other parameters being equal, significantly increases W_{p2} and V_{bl} (these increases are more significant the higher H is, as shown in Fig. 14); therefore, according to Eq. (19) F_{imp_max} also increases.

As a final consideration, it is highlighted how the combined use of diagrams generated by the theoretical calculation model, such as those in Figs. 14 and 16, can provide support for the definition of the main geometric parameters of the honeycomb (H and h_1/D), as the mass of the projectile varies, taking into account the effects on the honeycomb capacity of energy dissipation and the impact force transmitted to the panel. For example, considering that the impact force must be kept below a maximum value (which would correspond to complete perforation) equal to 1.5 kN (dotted line in Fig. 16), it is possible to obtain useful information for sizing the honeycomb, varying on the mass of the projectile:

- For m_p= 2.09 g, a honeycomb thickness H of about 25 mm is sufficient for the purpose, regardless of the value of h_1/D.
- For m_p= 4.08 g, in the first instance, it is necessary to increase the thickness H up to 35 mm. However, if it is also required to increase the energy absorption capacity by setting a high value of $h_1/D = 0.016$, to keep the impact force within the pre-set limit it is necessary to further increase the thickness H up to 40 mm. In this case, from the diagram in Fig. 14 it is possible to estimate a corresponding value of the honeycomb core dissipation W_{p2} of approximately 12 J, which becomes significant in the overall energy dissipation effect, to the benefit of the panel's resistance.
- For m_p= 7.06 g, to comply with the impact force limit, a minimum thickness $H = 50$ mm is needed. If it is also required to increase the energy absorption capacity by setting a higher value of h_1/D, a first solution consists in the dimensioning of the honeycomb with $h_1/D = 0.012$ and $H = 60$ mm, which corresponds to a value of core dissipation $W_{p2} = 15$ J. If a core with high dissipative capacity is required, it is possible to orient the selection towards $h_1/D = 0.016$, but this requires H values of at least 80 mm; this last solution would allow to set an honeycomb with an estimated energy absorption capacity of 35 J, becoming predominant in the energy dissipation of the entire sandwich, and a consequent substantial increase in the ballistic limit, above 250 m/s (Fig. 14).

4. Conclusions

The outcome of crushing tests under static conditions has showed that honeycomb sandwich panels exhibit a repeatable and stable behavior characterized by a pseudo-elastic phase, in which the stress increases linearly with the strain up to the beginning of instability, followed by a huge plateau stage where, during plastic deformation of the cells, stress remained almost constant. The final step is the densification phase, in which the stress sudden increases. The measured average values are reported in the following: peak stress 1.96 MPa, plateau stress 0.93 MPa, energy absorption efficiency 0.62, strain corresponding to maximum efficiency 65%, specific absorbed energy 0.60 J/dm^3.

The response of the honeycomb to impact tests, performed with spherical 8 mm diameter hardened steel impactors, has led to the identification of the ballistic limit, for the projectile at hand, close to 195 m/s. The experimental data from impact tests comply with the Recht-Ipson model by adopting 195 m/s ballistic limit, $p = 1.70$ as the exponent parameter and $a = 1$ proportionality coefficient, the latter being fully suitable for no-plugging perforation and no-plastic straining of the projectile.

Tests performed on facesheets-only specimens have evidenced that, for the adopted specimens and projectile, secondary role of the honeycomb is noticeable in the reduction of projectile velocity and, in turn, in the energy absorption. On the contrary, a crucial role of honeycomb was found in mitigating the force transmitted through the specimen, as its presence distributes the above decay of projectile velocity over an impact duration roughly ten times greater than that of facesheets-only specimens.

The energy conservation-based analytical model for the calculation of the ballistic limit was developed by formulating the energy dissipation terms based on the observation of the deformation and failure morphologies due to panel perforation, revealed by sectioning the specimens subjected to the experimental tests, and was calibrated by experimental data for the assumption in the setting of average flow stress of the materials, that is the mechanical property expressing their plastic behavior during the penetration process.

The model has allowed to evaluate in detail the effect of dissipation mechanisms due to honeycomb crushing, facesheets response to impact and penetration, and the interactions between their mechanisms. Despite considering the ranges of variation in the mechanical property data of the materials and the different assumptions for calculating the average flow stress, the theoretical results were found highly consistent with the experimental ones, concerning not only the ballistic limit, which was considered fully validated within the range of 190–203 m/s, with a deviation from the experimental value not exceeding ±4%, but also concerning the radial extent of first facesheet deformation, and the crushing strength of the honeycomb core, with deviations within 7% and 15%, respectively.

The analyses of dissipative effects across the three stages of the perforation process, and of maximum impact force transmitted to the panel during penetration, have allowed to outline the different role of honeycomb core in energy absorption and impact load attenuation, highlighting the potential effect of the core thickening and the increase in density of the honeycomb structure in terms of contribution to the overall resistance and mechanical response to high-velocity penetration of the sandwich panel.

CRediT authorship contribution statement

Raffaele Barbagallo: Writing – review & editing, Writing – original draft, Supervision, Methodology, Investigation, Formal analysis, Conceptualization. **Giuseppe Bua:** Writing – review & editing, Writing – original draft, Supervision, Methodology, Investigation, Formal analysis, Conceptualization. **Girolamo Costanza:** Writing – review & editing, Writing – original draft, Supervision, Methodology, Investigation, Formal analysis, Conceptualization. **Fabio Giudice:** Writing – review & editing, Writing – original draft, Supervision, Methodology, Investigation, Formal analysis, Conceptualization. **Giuseppe Mirone:** Writing – review & editing, Writing – original draft, Supervision, Methodology, Investigation, Formal analysis, Conceptualization. **Andrea Sili:** Writing

– review & editing, Writing – original draft, Supervision, Methodology, Investigation, Formal analysis, Conceptualization. **Maria Elisa Tata:** Writing – review & editing, Writing – original draft, Supervision, Methodology, Investigation, Formal analysis, Conceptualization.

Declaration of competing interest

The authors declare that they have no known competing financial interests or personal relationships that could have appeared to influence the work reported in this paper.

Data availability

Data will be made available on request.

References

[1] O.A. Ganilova, M.P. Cartmell, M.P. Kiley, Experimental investigation of the thermoelastic performance of an aerospace aluminium honeycomb composite panel, Compos. Struct. 257 (2021) 113159, https://doi.org/10.1016/j.compstruct.2020.113159.
[2] K. Liu, S. Zong, Y. Li, Z. Wang, Z. Hu, Z. Wang, Structural response of the U-type corrugated core sandwich panel used in the ship structures under the lateral quasi-static compression load, Mar. Struct. 84 (2022) 103198, https://doi.org/10.1016/j.marstruc.2022.103198.
[3] V. Birman, G.A. Kardomateas, Review of current trends in research and applications of sandwich structures, Compos. B: Eng. 142 (2018) 221–240, https://doi.org/10.1016/j.compositesb.2018.01.027.
[4] G. Savage, Development of penetration resistance in the survival cell of a Formula 1 racing car, Eng. Fail. Anal. 17 (2010) 116–127, https://doi.org/10.1016/j.engfailanal.2009.04.015.
[5] S.V. Rupani, S.S. Jani, G.D. Acharya, Design, modelling and manufacturing aspects of honeycomb sandwich structures: a review, IJSDR 2 (2016) 526–532, https://doi.org/10.1712/ijsdr.17013.
[6] G. Costanza, F. Giudice, A. Sili, M.E. Tata, Correlation modeling between morphology and compression behavior of closed-cell Al foams based on X-ray computed tomography observations, Metals 11 (2021) 1370, https://doi.org/10.3390/met11091370.
[7] M. Sun, D. Wowk, C. Mechefske, E. Alexander, I.Y. Kim, Surface and honeycomb core damage in adhesively bonded aluminum sandwich panels subjected to low-velocity impact, Compos. B: Eng. 230 (2022) 109506, https://doi.org/10.1016/j.compositesb.2021.109506.
[8] A. Montazeri, A. Rahmani, M. Safarabadi, Performance and damage mechanism assessment of sandwich composites with glass/kenaf/epoxy skins and a novel core using quasi-static penetration, J. Braz. Soc. Mech. Sci. Eng. 45 (2023) 256, https://doi.org/10.1007/s40430-023-04185-y.
[9] S. Karami, M. Haghighi-Yazdi, M. Safarabadi, Low-velocity impact behavior of 3D-printed sandwich panels with integrated composite face sheets, Adv. Eng. Mater. 27 (2025) 2401923, https://doi.org/10.1002/adem.202401923.
[10] S. Li, R. Yang, S. Sun, B. Niu, Advances in the analysis of honeycomb structures: a comprehensive review, Compos. B: Eng. 296 (2025) 112208, https://doi.org/10.1016/j.compositesb.2025.112208.
[11] Z. Wang, Recent advances in novel metallic honeycomb structure, Compos. B: Eng. 166 (2019) 731–741, https://doi.org/10.1016/j.compositesb.2019.02.011.
[12] W. Qi, Y. Zhang, Y. Zhang, H. Yan, Y. Liu, Z. Zhang, Advanced honeycomb structures for aerospace: multiscale mechanics, bio-inspired hierarchical design, and multi-physics coupling responses, Thin-Walled Struct. 218 (2026) 114132, https://doi.org/10.1016/j.tws.2025.114132.
[13] H. Yin, W. Zhang, L. Zhu, F. Meng, J. Liu, G. Wen, Review on lattice structures for energy absorption properties, Compos. Struct. 304 (2023) 116397, https://doi.org/10.1016/j.compstruct.2022.116397.
[14] M. He, W. Hu, A study on composite honeycomb sandwich panel structure, Mater. Des. 29 (2008) 709–713, https://doi.org/10.1016/j.matdes.2007.03.003.
[15] A.G. Hanssen, Y. Girard, L. Olovsson, T. Berstad, M. Langseth, A numerical model for bird strike of aluminium foam-based sandwich panels, Int. J. Impact Eng. 32 (2006) 1127–1144, https://doi.org/10.1016/j.ijimpeng.2004.09.004.
[16] M. Amraei, M. Shahravi, Z. Noori, A. Lenjani, Application of aluminium honeycomb sandwich panel as an energy absorber of high-speed train nose, J. Compos. Mater. 48 (2013) 1027–1037, https://doi.org/10.1177/0021998313482019.
[17] A. Cherniaev, R. Carriere, R. Cherniaev, New predictive models for ballistic limit of spacecraft sandwich panels subjected to hypervelocity impact, WIT Trans. Built Environ. 209 (2022) 97–101, https://doi.org/10.2495/HPSU220091.
[18] Y. Chen, Q.-G. He, X.-W. Chen, Numerical study on debris cloud and channeling effect of honeycomb sandwich shields under hypervelocity impact, Thin-Walled Struct. 191 (2023) 111052, https://doi.org/10.1016/j.tws.2023.111052.
[19] B. Chang, Z. Wang, G. Bi, Energy absorption and damage analysis of fragments in high-speed impact on composite honeycomb sandwich structures, Appl. Sci. 14 (2024) 7303, https://doi.org/10.3390/app14167303.
[20] J. Guo, Q. He, L. Li, J. Zhu, D. Yan, Ballistic resistance of a novel re-entrant auxetic honeycomb under in-plane high-velocity impact, J. Compos. Mater. 58 (2024) 1031–1049, https://doi.org/10.1177/00219983241233933.
[21] M. Lotfy, M. Ezzeldin, Double densification effects of a new enhanced auxetic steel system on mitigating severe explosion, Def. Tech. (2025), https://doi.org/10.1016/j.dt.2025.09.011.
[22] R.K. McFarland, Hexagonal cell structures under post-buckling axial load, AAIA J. 1 (1963) 1380–1385, https://doi.org/10.2514/3.1798.
[23] T. Wierzbicki, Crushing analysis of metal honeycombs, Int. J. Impact Eng. 1 (1983) 157–174, https://doi.org/10.1016/0734-743X(83)90004-0.
[24] E. Wu, W.-S. Jiang, Axial crush of metallic honeycombs, Int. J. Impact Eng. 19 (1997) 439–456, https://doi.org/10.1016/S0734-743X(97)00004-3.
[25] Q. Zhou, R.R. Mayer, Characterization of aluminum honeycomb material failure in large deformation compression, shear, and tearing, J. Eng. Mater. Technol. Trans. ASME 124 (2002) 412–420, https://doi.org/10.1115/1.1491575.
[26] D. Mohr, M. Doyoyo, Nucleation and propagation of plastic collapse bands in aluminum honeycomb, J. Appl. Phys. 94 (2003) 2262–2270, https://doi.org/10.1063/1.1592010.
[27] H. Yin, G. Wen, Theoretical prediction and numerical simulation of honeycomb structures with various cell specifications under axial loading, Int. J. Mech. Mater. Des. 7 (2011) 253–263, https://doi.org/10.1007/s10999-011-9163-5.
[28] W. Goldsmith, D.L. Louie, Axial perforation of aluminum honeycombs by projectiles, Int. J. Solids Struct. 32 (1995) 1017–1046, https://doi.org/10.1016/0020-7683(94)00188-3.
[29] W.E. Baker, T.C. Togami, J.C. Weydert, Static and dynamic properties of high-density metal honeycombs, Int. J. Impact Eng. 21 (1998) 149–163, https://doi.org/10.1016/S0734-743X(97)00040-7.
[30] H. Zhao, G. Gary, Crushing behaviour of aluminium honeycombs under impact loading, Int. J. Impact Eng. 21 (1998) 827–836, https://doi.org/10.1016/S0734-743X(98)00034-7.
[31] A. Kolopp, S. Rivallant, C. Bouvet, Experimental study of sandwich structures as armour against medium-velocity impacts, Int. J. Impact Eng. 61 (2013) 24–35, https://doi.org/10.1016/j.ijimpeng.2013.05.007.
[32] A. Alavi Nia, S.B. Razavi, G.H. Majzoobi, Ballistic limit determination of aluminum honeycombs – experimental study, Mat. Sci. Eng. A 488 (2008) 273–280, https://doi.org/10.1016/j.msea.2007.11.044.
[33] G.H. Liaghat, A. Alavi Nia, H.R. Daghyani, M. Sadighi, Ballistic limit evaluation for impact of cylindrical projectiles on honeycomb, Thin-Walled Struct. 48 (2010) 55–61, https://doi.org/10.1016/j.tws.2009.07.008.
[34] T. Thomas, G. Tiwari, Crushing behavior of honeycomb structure: a review, Int. J. Crashworthiness 24 (2019) 555–579, https://doi.org/10.1080/13588265.2018.1480471.
[35] G.G. Corbett, S.R. Reid, W. Johnson, Impact loading of plates and shells by free-flying projectiles: a review, Int. J. Impact Eng. 18 (1996) 141–230, https://doi.org/10.1016/0734-743X(95)00023-4.
[36] C.E. Anderson, Analytical models for penetration mechanics: a review, Int. J. Impact Eng. 108 (2017) 3–26, https://doi.org/10.1016/j.ijimpeng.2017.03.018.
[37] R.F. Recht, T.W. Ipson, Ballistic perforation dynamics, J. Appl. Mech. Trans. ASME 30 (1963) 384–390, https://doi.org/10.1115/1.3636566.
[38] M.S. Hoo Fatt, K. Park, Perforation of honeycomb sandwich plates by projectiles, Compos. - A: Appl. Sci. Manuf. 31 (2000) 889–899, https://doi.org/10.1016/S1359-835X(00)00021-X.
[39] V. Skvortsov, J. Kepler, E. Bozhevolnaya, Energy partition for ballistic penetration of sandwich panels, Int. J. Impact Eng. 28 (2003) 697–716, https://doi.org/10.1016/S0734-743X(02)00153-7.
[40] S. Feli, M.H. Namdari Pour, An analytical model for composite sandwich panels with honeycomb core subjected to high-velocity impact, Compos. B: Eng. 43 (2012) 2439–2447, https://doi.org/10.1016/j.compositesb.2011.11.028.
[41] A. Kolopp, R.A. Alvarado, S. Rivallant, C. Bouvet, Modeling impact on aluminum sandwich including velocity effects in honeycomb core, J. Sandw. Struct. Mater. 15 (2013) 733–757, https://doi.org/10.1177/1099636213501102.
[42] G. Sun, D. Chen, H. Wang, P.J. Hazell, Q. Li, High-velocity impact behaviour of aluminium honeycomb sandwich panels with different structural configurations, Int. J. Impact Eng. 122 (2018) 119–136, https://doi.org/10.1016/j.ijimpeng.2018.08.007.
[43] Q.N. Zhang, X.W. Zhang, G.X. Lu, D. Ruan, Ballistic impact behaviors of aluminum alloy sandwich panels with honeycomb cores, J. Sandw. Struct. Mater. 20 (2018) 861–884, https://doi.org/10.1177/109963621668216.
[44] S.B. Rayhan, M.U. Chowdhury, X. Pu, Ballistic impact response of reinforced honeycomb sandwich panels, IOP Conf. Ser. Mater. Sci. Eng. 1226 (2022) 012079, https://doi.org/10.1088/1757-899X/1226/1/012079.
[45] N. Khaire, G. Tiwari, V. Patel, M.A. Iqbal, Assessment of the ballistic response of honeycomb sandwich structures subjected to offset and normal impact, Def. Tech. 28 (2023) 56–73, https://doi.org/10.1016/j.dt.2022.12.018.
[46] N. Khaire, G. Tiwari, S. Rathod, M.A. Iqbal, A. Topa, Perforation and energy dissipation behaviour of honeycomb core cylindrical sandwich shell subjected to conical shape projectile at high velocity impact, Thin-Walled Struct. 171 (2022) 108724, https://doi.org/10.1016/j.tws.2021.108724.
[47] L. Li, F. Jia, L. Liu, R. Yu, Q. Zhang, L. Li, Response of aluminium honeycomb sandwich panels under combined shock and impact loading: experimental and numerical investigations, Thin-Walled Struct. 193 (2023) 111256, https://doi.org/10.1016/j.tws.2023.111256.
[48] W. Goldsmith, G.-T. Wang, K. Li, D. Crane, Perforation of cellular sandwich plates, Int. J. Impact Eng. 19 (1997) 361–379, https://doi.org/10.1016/S0734-743X(97)00003-1.

[49] G. Arquilla, A. Ceci, G. Costanza, M.E. Tata, Effect of the load application angle on the compressive behavior of Al honeycomb under combined normal–shear stress, Materials 16 (2023) 5462, https://doi.org/10.3390/ma16155462.
[50] M. Stanczak, T. Fras, L. Blanc, P. Pawlowski, A. Rusinek, Blast-induced compression of a thin-walled aluminum honeycomb structure – experiment and modeling, Metals 9 (2019) 1350, https://doi.org/10.3390/met9121350.
[51] A. Wilbert, W.Y. Yang, S. Kyriakides, J.F. Floccari, Buckling and progressive crushing of laterally loaded honeycomb, Int. J. Solids Struct. 48 (2011) 803–816, https://doi.org/10.1016/j.ijsolstr.2010.11.014.
[52] R. Dubey, R. Jayaganthan, D. Ruan, N.K. Gupta, N. Jones, R. Velmurugan, Ballistic perforation and penetration of 6xxx-series aluminium alloys: a review, Int. J. Impact Eng. 172 (2023) 104426, https://doi.org/10.1016/j.ijimpeng.2022.104426.
[53] Y. Wang, B. Su, S. Zhang, R. Ma, H. Liu, Z. Li, Ballistic impact behavior of AA6061 plates with different thicknesses impacted by hemispherical-nosed projectiles, Thin-Walled Struct. 209 (2025) 112876, https://doi.org/10.1016/j.tws.2024.112876.
[54] R.L. Woodward, S.J. Cimpoeru, A study of the perforation of aluminium laminated targets, Int. J. Impact Eng. 21 (1998) 117–131, https://doi.org/10.1016/S0734-743X(97)00034-1.
[55] A. Alavi Nia, G.R. Hoseini, Experimental study of perforation of multi-layered targets by hemispherical-nosed projectiles, Mater. Des. 32 (2011) 1057–1065, https://doi.org/10.1016/j.matdes.2010.07.001.
[56] T. Borvik, M. Langseth, O.S. Hopperstad, K.A. Malo, Perforation of 12mm thick steel plates by 20mm diameter projectiles with flat, hemispherical and conical noses – Part I: experimental study, Int. J. Impact Eng. 27 (2002) 19–35, https://doi.org/10.1016/S0734-743X(01)00034-3.
[57] R.L. Woodward, The penetration of metal targets by conical projectiles, Int. J. Mech. Sci. 20 (1978) 349–350, https://doi.org/10.1016/0020-7403(78)90038-3.
[58] T. Wierzbicki, Petalling of plates under explosive and impact loading, Int. J. Impact Eng. 22 (1999) 935–954, https://doi.org/10.1016/S0734-743X(99)00028-7.
[59] M.F. Asbhy, Materials Selection in Mechanical Design, Fourth ed, Butterworth-Heinemann, Burlington, MA, 2011.
[60] G.E. Dieter, Mechanical Metallurgy, Third ed, McGraw-Hill, New York, 1986.
[61] U.S. Lindholm, R.L. Bessey, G.V. Smith, Effect of strain rate on yield strength, tensile strength and elongation of three aluminium alloys, J. Mater. 6 (1971) 119–133.
[62] H. Zhao, I. Elnasri, S. Abdennadher, An experimental study on the behaviour under impact loading of metallic cellular materials, Int. J. Mech. Sci. 47 (2005) 757–774, https://doi.org/10.1016/j.ijmecsci.2004.12.012.
[63] S. Ryan, L.H. Nguyen, D. Gallardy, S.J. Cimpoeru, A scaling law for predicting the ballistic limit of aluminium alloy targets perforated in ductile hole formation, Int. J. Impact Eng. 116 (2018) 34–50, https://doi.org/10.1016/j.ijimpeng.2018.02.005.